Journal of Marine Science and Application (2025) 24: 1264-1278
https://doi.org/10.1007/s11804-025-00639-y

RESEARCH ARTICLE

Enhanced Fractional-Order Nonsingular Terminal Sliding Mode Control for Fully Submerged Hydrofoil Craft with Actuator Saturation

Hongmin Niu[1], Shiquan Zhao[2], Cristina I. Muresan[3] and Clara Mihaela Ionescu[4,5]

Received: 24 May 2024 / Accepted: 23 November 2024
© Harbin Engineering University and Springer-Verlag GmbH Germany, part of Springer Nature 2025

Abstract

This study introduces an enhanced adaptive fractional-order nonsingular terminal sliding mode controller (AFONTSMC) tailored for stabilizing a fully submerged hydrofoil craft (FSHC) under external disturbances, model uncertainties, and actuator saturation. A novel nonlinear disturbance observer modified by fractional-order calculus is proposed for flexible and less conservative estimation of lumped disturbances. An enhanced adaptive fractional-order nonsingular sliding mode scheme augmented by disturbance estimation is also introduced to improve disturbance rejection. This controller design only necessitates surpassing the estimation error rather than adhering strictly to the disturbance upper bound. Additionally, an adaptive fast-reaching law with a hyperbolic tangent function is incorporated to enhance the responsiveness and convergence rates of the controller, thereby reducing chattering. Furthermore, an auxiliary actuator compensator is developed to address saturation effects. The resultant closed system of the FSHC with the designed controller is globally asymptotically stable.

Keywords Fully submerged hydrofoil craft; Longitudinal motion control; Fractional-order terminal sliding mode control; Disturbance observer; Saturation compensation

1 Introduction

Over the past few years, significant advancements have been made in the development of surface vehicles, such as hydrofoil crafts, unmanned surface vehicles, planing boats, and hovercrafts (Wang et al., 2024). These vehicles have garnered extensive research attention, particularly in attitude control, path planning, and trajectory tracking (Wang et al., 2022; He et al., 2024). A fully submerged hydrofoil craft (FSHC) represents an advanced marine surface vehicle with high sailing speed, minimal resistance, and exceptional performance. Elevated above the water surface by lift force, the FSHC experiences reduced resistance and frictional drag. However, the absence of inherent restoring forces and moments compromises its stability, necessitating an effective control system for attitude stabilization. Given the limited coupling between lateral and longitudinal motions, this work focuses on stabilizing longitudinal motion and achieving precise tracking of the desired height of the FSHC during high-speed sea travel.

In recent years, considerable attention has been devoted to the motion control of the FSHC. The seakeeping performance of hydrofoil crafts has been extensively investigated utilizing regulators and Kalman filtering techniques, albeit predominantly in calm water conditions (Kim and Yamato, 2004). An optimal preview servo system integrating wave elevation prediction for feedforward control has been developed to eliminate the need for human operation of the FSHC (Kim and Yamato, 2002). Robust integral feedback control has been proposed to regulate slow-varying systems, and a state feedback control strategy coupled with a disturbance observer has been established for fast-varying

Article Highlights

- A nonlinear fractional disturbance observer is proposed for accurate estimation of lumped disturbances by integrating the nonlinear disturbance observer with fractional-order calculus.
- A modified fractional-order nonsingular terminal sliding surface is integrated with disturbance estimation to enhance disturbance rejection.
- An adaptive fast-reaching law of the controller is designed utilizing the hyperbolic tangent function for rapid convergence.
- An auxiliary compensation system is developed to address actuator saturation via the feedback channel.

✉ Hongmin Niu
niuhongmin@chd.edu.cn

[1] School of Electronics and Control Engineering, Chang'an University, Xi'an 710064, China

[2] College of Intelligent Systems Science and Engineering, Harbin Engineering University, Harbin 150001, China

[3] Department of Automation, Technical University of Cluj-Napoca, Cluj-Napoca 400114, Romania

[4] Research Group on Dynamical Systems and Control, Faculty of Engineering and Architecture, Ghent University, Gent 9052, Belgium

[5] Flanders Make Core Lab Engineering in Machineries, Intelligence, Robotics and Electromechanics, Gent 9052, Belgium

systems to ensure the course stability of the FSHC (Liu et al., 2017). A novel filter algorithm combines square-root cubature Kalman and smooth variable structure filtering for accurately estimating the state of the fully submerged hydrofoil craft has been studied (Niu and Liu, 2024). Additionally, a switched adaptive backstepping control scheme has been devised for FSHC, incorporating compound learning techniques to achieve precise tracking control on the horizontal plane. Moreover, a compound learning technique incorporating a fuzzy logic system and a disturbance observer has been introduced to mitigate uncertainties in the FSHC (Deng et al., 2020). Furthermore, a joint control method for the FSHC that combines linear–quadratic optimal control with sliding-mode control has been investigated (Liu et al., 2022). Deng et al. (2020) studied the tracking control of the FSHC using compound learning and fuzzy logic systems. Besides, various control strategies, including optimal control, PID control, and robust control, have been employed for the motion control of the FSHC (Ren et al., 2005; Zhang, 2016). However, controllers designed based on linearized models may yield unsatisfactory performance in terms of accuracy because of the inherent nonlinearities and uncertainties in the dynamic model. Research focusing on longitudinal motion control of the FSHC, particularly considering lumped disturbance and actuator saturation, remains scarce.

To enhance robust performance in the presence of unknown disturbances and parameter perturbations, numerous advanced methods have been introduced for the motion control of rigid objects. These methods include model predictive control (Li et al., 2016), neural network control, robust control, and sliding mode control (Li et al., 2013). Sliding mode control (SMC) has garnered significant attention owing to its versatility in managing strong nonlinear dynamics and intrinsic robustness to disturbances and unmodeled dynamics, all while maintaining a straightforward physical structure design. Its simplicity and ideal performance make it well-suited for nonlinear systems (Hu et al., 2021). To mitigate the rocking motion induced by ocean waves, a strategy integrating SMC with an output feedback H_∞ control algorithm has been investigated (Ren and Yang, 2005). Conventional SMC ensures the convergence of signals to the sliding surface, but it does not guarantee finite-time convergence of sliding variables. To address this limitation, a fast terminal sliding mode variable structure control strategy has been proposed to achieve rapid convergence (Elmokadem et al., 2016; Tran and Kang, 2016; Yang and Yan, 2016). Additionally, a nonsingular terminal SMC scheme incorporating adaptive neural networks has been proposed for trajectory tracking control of underactuated unmanned surface vehicles (Wu et al., 2023). Moreover, fractional-order calculus has been incorporated into the SMC strategy to augment the design flexibility of controllers beyond conventional methods (Melicio et al., 2010; Mujumdar et al., 2015; Yu et al., 2020). Fractional-order control outperforms the output feedback H_∞ control algorithm under identical dynamic conditions, streamlining parameter design (Ionescu et al., 2020). In pursuit of enhanced performance and robustness against disturbances, various fractional-order SMC strategies have been investigated (Hua, 2019; Sun, 2018; Yin et al., 2014). The combination of fractional calculus and terminal SMC has shown improved convergence precision across diverse systems, including chaotic systems, linear motors, and quadrotor UAVs (Wang et al., 2016; Ni et al., 2017). This approach has proven particularly efficient in nonlinear actuator control for mechatronic systems (Ionescu and Muresan, 2015). A practical adaptive fractional-order terminal SMC (FOTSMC) strategy has been proposed to attain heightened convergence precision in the tracking control of linear motors (Sun and Ma, 2017). In a related study (Labbadi et al., 2023), a novel fractional-order recursive integral terminal sliding mode has been designed for quadrotor systems that eliminate the reaching phase and guarantee finite-time convergence. Furthermore, a novel adaptive fractional-order nonsingular terminal sliding mode control (FONTSMC) strategy has been introduced for applications in robot manipulators and spacecraft (Wu and Huang, 2021; Alipour et al., 2022). Incorporating fractional derivatives into sliding surfaces offers enhanced degrees of freedom, rapid response, and robustness against disturbances. However, despite the robustness to disturbances exhibited by fast terminal sliding mode designed with fractional calculus, it is susceptible to compensation errors in disturbance estimation, leading to controller chattering.

The FSHC, as widely acknowledged, is susceptible to uncertain and time-varying environmental disturbances from waves, wind, currents, and other contributing factors. To effectively mitigate the effect of external disturbances without compromising system performance, nonlinear disturbance observers (NDOBs) have been introduced to estimate and compensate for disturbances during controller design. NDOBs exhibit rapid and exceptional performance by effectively compensating for disturbances via the feedforward channel. Consequently, observer-based strategies have been developed to address lumped uncertainties and simplify controller design (Chak et al., 2017; Lungu, 2020; Mohammadi et al., 2013). In contrast to robust controllers, which prioritize robustness at the expense of performance, disturbance observer-based controllers actively reject disturbances to maintain optimal controller performance.

The practical utilization of actuators is inevitably constrained by their inherent limitations. For instance, during high-speed navigation of the FSHC, the actuator saturation of the foil may ensue, resulting in performance degradation and instability. Therefore, incorporating actuator saturation into the control design procedure is crucial to enhance system performance. Various compensator design methods

have been proposed to address saturation effects (Hu et al., 2002; Tyan and Bernstein, 2010; Wang et al., 2021). The controller is primarily designed to meet performance requirements while overlooking the effect of actuator saturation nonlinearity. Subsequently, saturation compensation is devised and integrated into the control system. This approach ensures system performance and is adaptable across diverse control strategies. Based on this methodology, the anti-windup compensator is widely employed (Chen et al., 2009; Saqib et al., 2019).

In this study, we propose a novel enhanced adaptive fractional-order nonsingular terminal sliding mode control (AFONTSMC) strategy for longitudinal motion control of the FSHC in the presence of actuator saturation. Unlike prior research, our approach comprehensively addresses external disturbances, model uncertainties, and actuator saturations in the controller design. Compared with the methodology outlined by Wu and Huang (2021), an enhanced fractional-order nonsingular terminal sliding mode surface is designed by integrating a disturbance observer to compensate for lumped disturbances and mitigate the chattering phenomenon. Furthermore, unlike the methodology proposed by Alipour et al. (2022), a continuous hyperbolic tangent function is employed in the reaching law of the SMC, coupled with an adaptive law for parameter adjustment within the control strategy. As a result, the designed controller exhibits improved smoothness and robustness. This controller explicitly considers the foil saturation situation, which is overlooked in prior longitudinal motion control strategies for the FHSC. Finally, experimental investigations are executed to validate the efficacy of the proposed controller. The primary contribution of this work is summarized as follows:

1) A nonlinear fractional disturbance observer is proposed for accurate estimation of lumped disturbances. By integrating the nonlinear disturbance observer with fractional-order calculus, we mitigate observer conservatism while enhancing estimation accuracy.

2) In contrast to conventional approaches, a modified fractional-order nonsingular terminal sliding surface is integrated with disturbance estimation to enhance disturbance rejection. Consequently, the switching gain of the controller only needs to surpass disturbance estimation errors rather than adhere strictly to disturbance upper bounds. Smoother controller operation with reduced chattering is realized. An adaptive fast-reaching law of the controller is also designed utilizing the hyperbolic tangent function to achieve a fast convergence rate and high control accuracy.

3) An auxiliary compensation system based on the dynamic model of the FSHC is developed to address actuator saturation via the feedback channel. The closed-loop system, comprising the AFONTSMC with disturbance observer, saturation compensation, and parameter adaptive, demonstrates global asymptotic stability within finite time.

The remainder of the paper is structured as follows: Section 2 presents the fundamentals of fractional calculus and establishes the dynamic model of the FSHC. Section 3 details the AFONTSM controller design with saturation compensation and nonlinear disturbance observer. Section 4 discusses the simulation results. Section 5 concludes the paper.

2 Preliminaries

2.1 Preliminaries of fractional calculus

Fractional-order differentiation and integration represent generalizations of their integer-order counterparts, and they offer powerful tools to describe diverse characteristics. The definitions of fractional derivatives, which extend beyond the traditional integer-order calculus, exhibit unique characteristics. This section defines fractional calculus. The fundamental fractional-order operator is delineated as follows. For detailed definitions of the Riemann Liouville fractional-order integration and Caputo's fractional derivative, readers are referred to Alipour et al. (2022).

$$\mathrm{D}_t^{\alpha}=\begin{cases}\dfrac{\mathrm{d}^{\alpha}}{\mathrm{d}t^{\alpha}} & \alpha>0\\ 1 & \alpha=0\\ \displaystyle\int_{t_0}^{t}(\mathrm{d}\tau)^{-\alpha} & \alpha<0\end{cases} \tag{1}$$

where α is the fractional order. The correlation lemmas are given as follows:

1) Lemma 1 (Alipour et al., 2022). The operator ${}_a\mathrm{I}_t^{\gamma}=\dfrac{1}{\Gamma(\gamma)}\displaystyle\int_a^t\frac{\delta(\tau)}{(t-\tau)^{1-\gamma}}\mathrm{d}\tau$ is bounded in $L_p(\hat{a},\hat{b})$ when satisfied $\left(t>a;\delta\in C,\mathrm{Re}(\delta)>0\right)\left(1\leqslant p\leqslant\infty,-\infty<\bar{c}<\bar{d}<\infty\right)$:

$$\left\|{}_a\mathrm{I}_t^{\gamma}\delta\right\|_p\leqslant K\left\|\delta\right\|_p,\left(K=\frac{(\bar{d}-\bar{c})^{\mathrm{Re}(\gamma)}}{\mathrm{Re}(\gamma)\left|\Gamma(\gamma)\right|}\right) \tag{2}$$

2) Lemma 2 (Wu and Huang, 2021). Considering the sign function and the RL fractional derivative operator $\mathrm{D}_t^{\alpha}\delta(t)=\dfrac{1}{\Gamma(1-\alpha)}\dfrac{\mathrm{d}}{\mathrm{d}t}\displaystyle\int_0^t\frac{\delta(\tau)}{(t-\tau)^{\alpha}}\mathrm{d}\tau$, $0\leqslant\alpha<1$, we can derive

$$\mathrm{D}_t^{\alpha}\,\mathrm{sgn}\,(e(t))\begin{cases}>0 & \text{if } e(t)>0,t>0\\ <0 & \text{if } e(t)<0,t<0\end{cases} \tag{3}$$

2.2 Dynamic model of the FSHC

We focus on the longitudinal motion of the FSHC, which encompasses pitch angle and heave motion. Figure 1 pres-

ents the overall structural configuration of the FSHC (Liu et al., 2019a).

The FSHC model, integrating translational and rotational motions, is built upon the principles of rigid body dynamics. Given the momentum theorems and rigid body dynamics, the dynamic model of the FSHC moving at constant speed with small perturbations is established as follows:

$$\begin{cases} m\left[\dot{\boldsymbol{V}} + \boldsymbol{\Omega}\boldsymbol{V}_e + \dot{\boldsymbol{\Omega}}\boldsymbol{R}_G\right] = \boldsymbol{F} \\ \boldsymbol{I}\dot{\boldsymbol{w}} + \boldsymbol{R}_G\left[\dot{\boldsymbol{V}} + \boldsymbol{\Omega}\boldsymbol{V}_e\right]m = \boldsymbol{M} \end{cases} \tag{4}$$

where $\boldsymbol{V} = \begin{bmatrix} u \\ v \\ w \end{bmatrix}$ represents the velocity vector, $\boldsymbol{V}_e = \begin{bmatrix} u_e \\ 0 \\ 0 \end{bmatrix}$ is the constant speed under small perturbation, $\boldsymbol{\Omega} = \begin{bmatrix} 0 & -r & q \\ r & 0 & -p \\ -q & p & 0 \end{bmatrix}$ denotes the rotation transform matrix, $\boldsymbol{F} = \begin{bmatrix} X \\ Y \\ Z \end{bmatrix}$ is the force, $\boldsymbol{I} = \begin{bmatrix} I_X & 0 & 0 \\ 0 & I_Y & 0 \\ 0 & 0 & I_Z \end{bmatrix}$ represents the inertia moment, $\boldsymbol{w} = \begin{bmatrix} p \\ q \\ r \end{bmatrix}$ denotes the angle velocity, $\boldsymbol{M} = \begin{bmatrix} K \\ M \\ N \end{bmatrix}$ represents the moment vector, and $\boldsymbol{R}_G = \begin{bmatrix} 0 & -z_G & y_G \\ z_G & 0 & -x_G \\ -y_G & x_G & 0 \end{bmatrix}$ denotes the location transform matrix about the center of gravity. Table 1 provides the definitions of the motion variables.

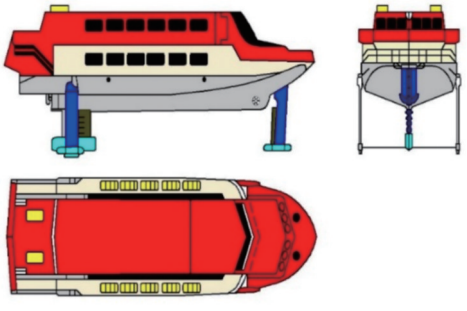

Figure 1 Overall shape structure of the FSHC

Table 1 6-DOF motion of the FSHC

Direction of motion	Force/moment	Velocity	Displacement
Translational along *X*-axes	*X*	*u*	*x*
Translational along *Y*-axes	*Y*	*v*	*y*
Translational along *Z*-axes	*Z*	*w*	*z*
Rotate along *X*-axes	*K*	*p*	φ
Rotate along *Y*-axes	*M*	*q*	θ
Rotate along *Z*-axes	*N*	*r*	ψ

The disturbance force and moment are composed of hydrodynamic and wave forces and moments induced by irregular waves. The total force and moment can be expressed as

$$\boldsymbol{F} = \left(\frac{\partial \boldsymbol{F}}{\partial \boldsymbol{V}}\right)\boldsymbol{V} + \left(\frac{\partial \boldsymbol{F}}{\partial \dot{\boldsymbol{V}}}\right)\dot{\boldsymbol{V}} + \left(\frac{\partial \boldsymbol{F}}{\partial \boldsymbol{w}}\right)\boldsymbol{w} + \left(\frac{\partial \boldsymbol{F}}{\partial \dot{\boldsymbol{w}}}\right)\dot{\boldsymbol{w}} + \left(\frac{\partial \boldsymbol{F}}{\partial \boldsymbol{g}}\right)\boldsymbol{g} + \left(\frac{\partial \boldsymbol{F}}{\partial \boldsymbol{Z}}\right)\boldsymbol{Z} + \left(\frac{\partial \boldsymbol{F}}{\partial \boldsymbol{\delta}}\right)\boldsymbol{\delta} + \boldsymbol{F}_S \tag{5}$$

$$\boldsymbol{M} = \left(\frac{\partial \boldsymbol{M}}{\partial \boldsymbol{V}}\right)\boldsymbol{V} + \left(\frac{\partial \boldsymbol{M}}{\partial \dot{\boldsymbol{V}}}\right)\dot{\boldsymbol{V}} + \left(\frac{\partial \boldsymbol{M}}{\partial \boldsymbol{w}}\right)\boldsymbol{w} + \left(\frac{\partial \boldsymbol{M}}{\partial \dot{\boldsymbol{w}}}\right)\dot{\boldsymbol{w}} + \left(\frac{\partial \boldsymbol{M}}{\partial \boldsymbol{g}}\right)\boldsymbol{g} + \left(\frac{\partial \boldsymbol{M}}{\partial \boldsymbol{Z}}\right)\boldsymbol{Z} + \left(\frac{\partial \boldsymbol{M}}{\partial \boldsymbol{\delta}}\right)\boldsymbol{\delta} + \boldsymbol{M}_S \tag{6}$$

where $\frac{\partial \boldsymbol{F}}{\partial \boldsymbol{V}} = \begin{bmatrix} X_u & X_v & X_w \\ Y_u & Y_v & Y_w \\ Z_u & Z_v & Z_w \end{bmatrix}$, $\frac{\partial \boldsymbol{F}}{\partial \dot{\boldsymbol{V}}} = \begin{bmatrix} X_{\dot{u}} & X_{\dot{v}} & X_{\dot{w}} \\ Y_{\dot{u}} & Y_{\dot{v}} & Y_{\dot{w}} \\ Z_{\dot{u}} & Z_{\dot{v}} & Z_{\dot{w}} \end{bmatrix}$, $\frac{\partial \boldsymbol{F}}{\partial \dot{\boldsymbol{w}}} = \begin{bmatrix} X_{\dot{p}} & X_{\dot{q}} & X_{\dot{r}} \\ Y_{\dot{p}} & Y_{\dot{q}} & Y_{\dot{r}} \\ Z_{\dot{p}} & Z_{\dot{q}} & Z_{\dot{r}} \end{bmatrix}$, $\frac{\partial \boldsymbol{F}}{\partial \boldsymbol{g}} = \begin{bmatrix} X_\phi & X_\theta & X_\psi \\ Y_\phi & Y_\theta & Y_\psi \\ Z_\phi & Z_\theta & Z_\psi \end{bmatrix}$, $\boldsymbol{g} = \begin{bmatrix} \phi \\ \theta \\ \psi \end{bmatrix}$, $\frac{\partial \boldsymbol{F}}{\partial \boldsymbol{\delta}} = \begin{bmatrix} X_\delta \\ Y_\delta \\ Z_\delta \end{bmatrix}$, $\frac{\partial \boldsymbol{F}}{\partial \boldsymbol{Z}} = \begin{bmatrix} X_z \\ Y_Z \\ Z_Z \end{bmatrix}$.

δ is the flap angle, $\frac{\partial \boldsymbol{F}}{\partial \boldsymbol{V}}$ is the derivative of the hydrodynamic force with respect to the velocity of each axis, and $\frac{\partial \boldsymbol{F}}{\partial \dot{\boldsymbol{V}}}$ represents the derivative of the hydrodynamic force with respect to acceleration. Similarly, other derivatives are defined. $\boldsymbol{F}_S = \begin{bmatrix} X_S & Y_S & Z_S \end{bmatrix}^{\mathrm{T}}$ and $\boldsymbol{M}_S = \begin{bmatrix} K_S & M_S & N_S \end{bmatrix}^{\mathrm{T}}$ are the disturbance force and moment, respectively.

We then substitute Equations (5) and (6) into (4) and consider $R_G = 0$, $v_e = w_e = 0$, $\dot{u} = 0$, and $\psi = 0$. Thus, the longitudinal motion equations of the FSHC can be obtained by expanding Equation (4) by the matrix defined above and considering the heave motion and pitch motion. The relationship between the earth-fixed and body-fixed frames (Fossen, 1994) is considered:

$$\begin{bmatrix} \dot{z} \\ \dot{\theta} \end{bmatrix} = \begin{bmatrix} \cos\theta & 0 \\ 0 & 1 \end{bmatrix}\begin{bmatrix} w \\ q \end{bmatrix} + \begin{bmatrix} -u_e \sin\theta \\ 0 \end{bmatrix} \tag{7}$$

where w denotes the heave velocity and q is the pitch angle velocity in the body-fixed frame. $\dot{z}$ and $\dot{\theta}$ denote the heave velocity and pitch angle velocity, respectively. The nonlinear dynamic model of the FSHC, accounting for external disturbances and parameter perturbations, is established as described by Liu et al. (2019a; 2019b):

$$\left(Z_{\dot{w}} - m\right)\dot{w} + Z_w w + Z_z z + Z_{\dot{q}}\dot{q} + \left(Z_q + u_e m\right)q + Z_\theta \theta = -Z_{\delta_a}\delta_a - Z_{\delta_b}\delta_b - Z_S \tag{8}$$

$$M_{\dot{w}}\dot{w} + M_w w + M_z z + (M_{\dot{q}} - I_y)\dot{q} + M_q q + M_\theta \theta = - M_{\delta_a}\delta_a - M_{\delta_b}\delta_b - M_S \tag{9}$$

Considering (7), we convert the FSHC model presented in Equations (8) and (9) into the following state-space function:

$$\begin{cases} \dot{\boldsymbol{x}}_1 = \boldsymbol{x}_2 \\ \dot{\boldsymbol{x}}_2 = \bar{\boldsymbol{f}}_1(\boldsymbol{x}_1, \boldsymbol{x}_2) + \bar{\boldsymbol{f}}_2(\boldsymbol{x}_1, \boldsymbol{x}_2) + \boldsymbol{B}\boldsymbol{u} + \boldsymbol{d}_w \end{cases} \tag{10}$$

$$\bar{\boldsymbol{f}}_1 = \begin{bmatrix} \left(\frac{a_3 b_3 - a_2}{1 - a_3 b_1}\right) z - \left(\frac{a_3 b_5 - a_5}{1 - a_3 b_1}\right)\theta - \frac{1}{\cos\theta}\left(\frac{a_3 b_2 - a_1}{1 - a_3 b_1}\right)\dot{z} - \left(\frac{a_3 b_4 - a_4}{1 - a_3 b_1}\right)\dot{\theta} \\ \left(\frac{a_2 b_1 - b_3}{1 - a_3 b_1}\right) z - \left(\frac{a_5 b_1 - b_5}{1 - a_3 b_1}\right)\theta - \frac{1}{\cos\theta}\left(\frac{a_1 b_1 - b_2}{1 - a_3 b_1}\right)\dot{z} - \left(\frac{a_4 b_1 - b_4}{1 - a_3 b_1}\right)\dot{\theta} \end{bmatrix} \tag{11}$$

$$\bar{\boldsymbol{f}}_2 = \begin{bmatrix} \left(\frac{a_3 b_2 - a_1}{1 - a_3 b_1}\right) u_e \tan\theta & \left(\frac{a_1 b_1 - b_2}{1 - a_3 b_1}\right) u_e \tan\theta \end{bmatrix}^{\mathrm{T}} \tag{12}$$

where $a_1 = \frac{Z_w}{\left(Z_{\dot{w}} - m_1\right)}$, $a_2 = \frac{Z_z}{\left(Z_{\dot{w}} - m_1\right)}$, $a_3 = \frac{Z_{\dot{q}}}{\left(Z_{\dot{w}} - m_1\right)}$, $a_4 = \frac{\left(Z_q + U_e m_1\right)}{\left(Z_{\dot{w}} - m_1\right)}$, $a_5 = \frac{Z_\theta}{\left(Z_{\dot{w}} - m_1\right)}$, $a_6 = \frac{Z_{\delta_e}}{\left(Z_{\dot{w}} - m_1\right)}$, $a_7 = \frac{Z_{\delta_f}}{\left(Z_{\dot{w}} - m_1\right)}$, $a_8 = 1$, $b_1 = \frac{M_{\dot{w}}}{\left(M_{\dot{q}} - I_y\right)}$, $b_2 = \frac{M_w}{\left(M_{\dot{q}} - I_y\right)}$, $b_3 = \frac{M_z}{\left(M_{\dot{q}} - I_y\right)}$, $b_4 = \frac{M_q}{\left(M_{\dot{q}} - I_y\right)}$, $b_5 = \frac{M_\theta}{\left(M_{\dot{q}} - I_y\right)}$, $b_6 = \frac{M_{\delta e}}{\left(M_{\dot{q}} - I_y\right)}$, $b_7 = \frac{M_{\delta f}}{\left(M_{\dot{q}} - I_y\right)}$, $b_8 = 1$.

where $\boldsymbol{x}_1 = \left[z, \theta\right]^{\mathrm{T}}$ is the system state vector, $\bar{\boldsymbol{f}}_1(\boldsymbol{x}_1, \boldsymbol{x}_2)$ and $\bar{\boldsymbol{f}}_2(\boldsymbol{x}_1, \boldsymbol{x}_2)$ are nominal nonlinear items, and $\boldsymbol{d}_w = \Delta\boldsymbol{f}_1(\boldsymbol{x}_1, \boldsymbol{x}_2) + \Delta\boldsymbol{f}_2(\boldsymbol{x}_1, \boldsymbol{x}_2) + \boldsymbol{d}_1$ is the lumped disturbance. $\hat{\Delta}\boldsymbol{f}_1(\boldsymbol{x}_1, \boldsymbol{x}_2)$ and $\hat{\Delta}\boldsymbol{f}_2(\boldsymbol{x}_1, \boldsymbol{x}_2)$ represent the parameter perturbations, and $\boldsymbol{d}_1$ is the external disturbance caused by waves and wind. $\boldsymbol{u} = \left[\delta_a, \delta_b\right]^{\mathrm{T}} \in R^2$ is the control item.

Assumption 1. The nonlinear parts of $\bar{\boldsymbol{f}}_1(\boldsymbol{x}_1, \boldsymbol{x}_2)$ and $\bar{\boldsymbol{f}}_2(\boldsymbol{x}_1, \boldsymbol{x}_2)$ are continuously differentiable and locally Lipschitz.

Assumption 2. The lumped disturbance $\boldsymbol{d}_w$ is limited as $\left\|\boldsymbol{d}_w\right\| < W$, and its derivative is bounded as $\left\|\dot{\boldsymbol{d}}_w\right\| < \bar{W}$.

3 AFONTSM controller design

The control objective of the FSHC is for the state $\boldsymbol{x}_1 = \left[z, \theta\right]^{\mathrm{T}}$ of heave motion and pitch angle to approach the equilibrium point $\boldsymbol{x}_d = \left[z_d, \theta_d\right]^{\mathrm{T}}$ in the presence of lumped disturbance and actuator saturation. The nonlinear disturbance observer is designed to estimate the lumped disturbance, and the anti-windup compensator is devised to compensate for the influence of the actuator saturation. Thus, the AFONTSMC is developed for longitudinal motion control of the FSHC under actuator saturation and disturbances with a fast convergence rate and high control accuracy.

The aim of the control strategy is to improve the performance of the controller working in the outer control loop with the disturbance observer and actuator compensator operating in the inner loop. Figure 2 depicts the diagram of the designed control system.

3.1 Nonlinear disturbance observer with fractional-order calculus

Considering the influence of ocean wave disturbances and model uncertainties on controller performance, we design a nonlinear disturbance observer incorporating fractional-order calculus to estimate lumped disturbances. The design minimizes conversation and system limitations, so the observer can be utilized in controller design for disturbance compensation.

$$\boldsymbol{H} = \dot{\boldsymbol{e}}_1 + \lambda_1 \mathrm{D}^{\alpha - 1}\left(\mathrm{sig}^{\lambda_2}(\boldsymbol{e}_1)\right) \tag{13}$$

$$\begin{cases} \hat{\boldsymbol{d}}_w = \boldsymbol{L} + \boldsymbol{g}\boldsymbol{H} \\ \dot{\boldsymbol{L}} = -\boldsymbol{g}\left[\bar{\boldsymbol{f}}_1(\boldsymbol{x}_1, \boldsymbol{x}_2) + \bar{\boldsymbol{f}}_2(\boldsymbol{x}_1, \boldsymbol{x}_2) + \boldsymbol{B}\boldsymbol{u} + \boldsymbol{L} + \boldsymbol{g}\boldsymbol{H} + \lambda_1 \mathrm{D}^{\alpha}\left(\mathrm{sig}^{\lambda_2}(\boldsymbol{e}_1)\right)\right] \end{cases} \tag{14}$$

The nonlinear disturbance observer is formulated in Equation (14), with $\boldsymbol{H}$ as the nonlinear function designed with fractional-order calculus. The derivative of $\boldsymbol{H}$ is obtained as $\dot{\boldsymbol{H}} = \ddot{\boldsymbol{e}}_1 + \lambda_1 \mathrm{D}^{\alpha}\left(\mathrm{sig}^{\lambda_2}(\boldsymbol{e}_1)\right)$. $\boldsymbol{e}_1 = \boldsymbol{x}_1 - \boldsymbol{x}_d$ represents the state error, $\boldsymbol{x}_d = \left[0, 0\right]^{\mathrm{T}}$ represents the desired state, $\hat{\boldsymbol{d}}_w$ denotes the estimation of the lumped disturbance, and $\boldsymbol{L}$ represents the internal state. The fractional operator is constrained within the range $0 < \alpha < 1$, with $\boldsymbol{g} = \mathrm{diag}(g_1, g_2)$, λ_1, and λ_2 being positive parameters.

Differentiating (13) and (14), considering the model of the FSHC, and using the definitions and lemmas of fractional-order derivative, we can obtain $\dot{\hat{\boldsymbol{d}}}_w$ as follows:

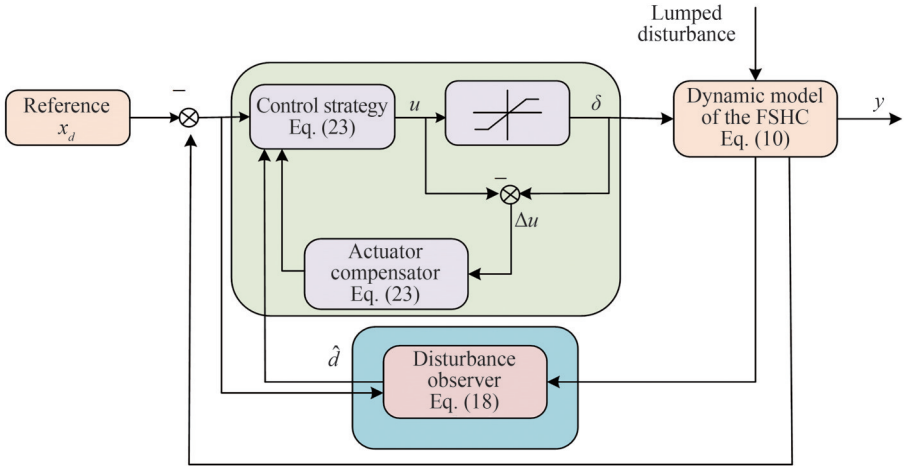

Figure 2 Proposed diagram of the designed control system

$$\begin{aligned}\dot{\hat{\boldsymbol{d}}}_w &= \dot{\boldsymbol{L}} + \boldsymbol{g}\dot{\boldsymbol{H}} = -\boldsymbol{g}\left[\bar{\boldsymbol{f}}_1(\boldsymbol{x}_1,\boldsymbol{x}_2) + \bar{\boldsymbol{f}}_2(\boldsymbol{x}_1,\boldsymbol{x}_2) + \right.\\ &\left.\boldsymbol{B}\boldsymbol{u} + \boldsymbol{L} + \boldsymbol{g}\boldsymbol{H} + \lambda_1 \mathrm{D}^{\alpha}\left(\mathrm{sig}^{\lambda_2}(\boldsymbol{e}_1)\right)\right] + \\ &\boldsymbol{g}\left(\ddot{\boldsymbol{e}}_1 + \lambda_1 \mathrm{D}^{\alpha}\left(\mathrm{sig}^{\lambda_2}(\boldsymbol{e}_1)\right)\right) = \\ &-\boldsymbol{g}\left[\bar{\boldsymbol{f}}_1(\boldsymbol{x}_1,\boldsymbol{x}_2) + \bar{\boldsymbol{f}}_2(\boldsymbol{x}_1,\boldsymbol{x}_2) + \right.\\ &\left.\boldsymbol{B}\boldsymbol{u} + \boldsymbol{L} + \boldsymbol{g}\boldsymbol{H} + \lambda_1 \mathrm{D}^{\alpha}\left(\mathrm{sig}^{\lambda_2}(\boldsymbol{e}_1)\right)\right] + \\ &g\left(\bar{\boldsymbol{f}}_1(\boldsymbol{x}_1,\boldsymbol{x}_2) + \bar{\boldsymbol{f}}_2(\boldsymbol{x}_1,\boldsymbol{x}_2) + \boldsymbol{B}\boldsymbol{u} + \boldsymbol{d}_w + \right.\\ &\left.\lambda_1 \mathrm{D}^{\alpha}\left(\mathrm{sig}^{\lambda_2}(\boldsymbol{e}_1)\right)\right) = -\boldsymbol{g}\boldsymbol{L} - \boldsymbol{g}\left(\boldsymbol{g}\boldsymbol{H}\right) + \boldsymbol{g}\boldsymbol{d}_w = \\ &\boldsymbol{g}\left(\boldsymbol{d}_w - \hat{\boldsymbol{d}}_w\right) = \boldsymbol{g}\tilde{\boldsymbol{d}}_w \end{aligned} \tag{15}$$

The convergence rate of the estimation error is influenced by g, underscoring the importance of selecting an appropriate value for this parameter. The nonlinear disturbance observer with fractional-order components designed in Equation (14) ensures the boundedness of the estimation error within finite time. Furthermore, effective compensation for the estimation error is achievable through the controller.

3.2 Anti-windup compensator design

Actuator saturation is a common occurrence in industrial manufacturing, often resulting in serious deterioration of the controller's performance. The flap angle of the FSHC is limited, so the effect of actuator saturation should be taken into account during controller design. The model of the FSHC considering actuator saturation can be expressed as

$$\begin{cases}\dot{\boldsymbol{x}}_1 = \boldsymbol{x}_2 \\ \dot{\boldsymbol{x}}_2 = \boldsymbol{f}_1(\boldsymbol{x}_1,\boldsymbol{x}_2) + \boldsymbol{f}_2(\boldsymbol{x}_1,\boldsymbol{x}_2) + \boldsymbol{B}\boldsymbol{\delta} + \boldsymbol{d}_w\end{cases} \tag{16}$$

where $\boldsymbol{\delta} = [\delta_a \quad \delta_b]^{\mathrm{T}}$ denotes the aft flap angle and bow flap angle of the FSHC, respectively.

$$\delta_i = \mathrm{sat}(u_i) = \begin{cases}\delta_{i\max} & u_i > \delta_{i\max} \\ u_i & \delta_{i\min} < u_i < \delta_{i\max} \\ \delta_{i\min} & u_i < \delta_{i\min}\end{cases} \tag{17}$$

To mitigate the effects of actuator saturation, an anti-windup compensator is designed, which incorporates the structural characteristics of the flap actuators and the physical dynamic behavior of the FSHC. When actuator saturation occurs, the anti-windup compensator is activated to reduce the effects of this saturation. This compensator is designed independently of the controller specifically to handle the issue of constraints and maintain the stability of the control system (Tarbouriech and Turner, 2009; Chen et al., 2011). The anti-windup compensator with fractional-order components is designed as follows:

$$\dot{\boldsymbol{\varphi}} = \begin{cases} -k_3\boldsymbol{\varphi} - \dfrac{\left\|\boldsymbol{S}^{\mathrm{T}}\mathrm{D}^{\alpha-1}(\boldsymbol{B}\Delta\boldsymbol{u})\right\| + 1/2\rho^2(\Delta\boldsymbol{u})^{\mathrm{T}}\Delta\boldsymbol{u}}{\left\|\boldsymbol{\varphi}\right\|^2}\boldsymbol{\varphi} + \rho\Delta\boldsymbol{u} & \left\|\boldsymbol{\delta}\right\| > \tau \\ 0 & \left\|\boldsymbol{\delta}\right\| < \tau \end{cases} \tag{18}$$

where $\Delta\boldsymbol{u} = \boldsymbol{\delta} - \boldsymbol{u}$, $\boldsymbol{\varphi}$ denotes the state of the actuator compensation system, $k_3 > 1$ and $\rho > 0$ are the parameters to be selected, and τ is an arbitrary small constant.

3.3 AFONTSM controller design

An AFONTSMC is designed for the longitudinal motion

control of the FSHC. A novel sliding mode surface modified by a disturbance observer is introduced to enhance the controller's performance under lumped disturbances. Instead of using the sign function, a hyperbolic tangent function is employed in the reaching law of the SMC. Additionally, an adaptive law is incorporated to manage uncertain parameters within the control strategy.

To reduce the effect of disturbances further, a fractional-order fast terminal sliding mode surface is designed by integrating the disturbance observer as follows:

$$\boldsymbol{S}(t) = \mathrm{D}^{\alpha-1}\dot{\boldsymbol{e}}_1(t) + \chi \boldsymbol{e}_1(t) + \beta \boldsymbol{e}_1(t)^{(p/q)} + \lambda \hat{\boldsymbol{d}}_w \quad (19)$$

where $\boldsymbol{S}(t) = \begin{bmatrix} s_1 & s_2 \end{bmatrix}^{\mathrm{T}}$, and $\chi \in R^{2\times 2}$ represents the constant matrix to be selected. λ is the parameter to be selected, $\beta > 0$ is a constant parameter, and $0 < \alpha < 1$. p and q are odd integers such that $0 < p < q < 2p$. To ensure fast convergence while considering the model and system characteristics of the FSHC, the parameter is typically selected as $p = 3$ and $q = 5$.

Remark 1. The fractional-order sliding mode surface, as designed in Equation (19), is modified by incorporating a disturbance observer. Although most existing works focus on incorporating state error considerations when designing sliding surfaces, the estimation error of disturbances is seldom accounted for in designing fractional-order sliding mode surfaces. We effectively mitigate the effect of lumped disturbances on the controller by introducing a sliding mode surface based on disturbance estimation. Consequently, the switching gain of control law only needs to exceed the disturbance error instead of the disturbance upper bound. The utilization of fractional calculus, as employed in Equation (19), reduces the controller's reliance on an accurate model and conservatism. This approach addresses chattering issues associated with sliding mode controllers and ensures that no adverse effects are caused by incorporating a disturbance observer.

Differentiating (19), we can derive

$$\begin{aligned}
\dot{\boldsymbol{S}}(t) &= \mathrm{D}^{\alpha-1}\ddot{\boldsymbol{e}}_1(t) + \chi\dot{\boldsymbol{e}}_1(t) + \beta\frac{p}{q}\boldsymbol{e}_1(t)^{(p/q-1)}\dot{\boldsymbol{e}}_1(t) + \lambda\dot{\hat{\boldsymbol{d}}}_w \\
&= \mathrm{D}^{\alpha-1}(\ddot{\boldsymbol{x}}_1 - \ddot{\boldsymbol{x}}_d) + \chi\dot{\boldsymbol{e}}_1(t) + \beta\frac{p}{q}\boldsymbol{e}_1(t)^{(p/q-1)}\dot{\boldsymbol{e}}_1(t) + \lambda\dot{\hat{\boldsymbol{d}}}_w \\
&= \mathrm{D}^{\alpha-1}\left(\bar{\boldsymbol{f}}_1(\boldsymbol{x}_1,\boldsymbol{x}_2) + \bar{\boldsymbol{f}}_2(\boldsymbol{x}_1,\boldsymbol{x}_2) + \boldsymbol{B}\boldsymbol{\delta} + \boldsymbol{d}_w\right) + \\
&\quad \chi\dot{\boldsymbol{e}}_1(t) + \beta\frac{p}{q}\boldsymbol{e}_1(t)^{(p/q-1)}\dot{\boldsymbol{e}}_1(t) + \lambda g\tilde{\boldsymbol{d}}_w
\end{aligned} \quad (20)$$

To achieve fast convergence and high tracking precision in the existence of complex lumped disturbances, a novel adaptive fast-reaching law with a continuous hyperbolic tangent function is designed as follows:

$$\dot{\boldsymbol{S}}(t) = -\boldsymbol{K}_1|\boldsymbol{S}|^m\mathrm{sgn}(\boldsymbol{S}) - \boldsymbol{K}_2|\boldsymbol{S}|^n\mathrm{sgn}(\boldsymbol{S}) - \hat{K}\tanh\left(\frac{\boldsymbol{S}}{\boldsymbol{\varepsilon}}\right) \quad (21)$$

where $\boldsymbol{K}_1 = \mathrm{diag}(k_{a1}, k_{b1})$ and $\boldsymbol{K}_2 = \mathrm{diag}(k_{a2}, k_{b2})$ are positive constant matrices. $\hat{K}$ is the time-varying parameter to be designed by the adaptive law. $0 < m < 1$ and $n > 1$ are positive constants, and $\tanh(\boldsymbol{S}) = \begin{bmatrix}\tanh(s_1) & \tanh(s_2)\end{bmatrix}^{\mathrm{T}}$.

Remark 2. In contrast to previous studies, the adaptive fast-reaching law designed in Equation (21) comprises two parts that greatly reduce chattering and enable a faster response. The power reaching law accelerates convergence to the sliding mode when the system state is far from it while exhibiting a smaller gain as the state approaches the sliding mode surface. Additionally, the continuous hyperbolic tangent function is introduced to mitigate the effect of disturbances and ensure smoother controller operation. The adaptive fast-reaching law design guarantees the mitigation of lumped disturbances.

Lemma 3. Considering the hyperbolic tangent function, for any $\chi \in R$, $\varepsilon > 0$ exists, thus satisfying the following inequality:

$$0 \leqslant |\chi| - \chi\tanh(\chi/\varepsilon) \leqslant \mu\varepsilon, \mu = 0.278\,5 \quad (22)$$

We then design the AFONTSMC with a disturbance observer to guarantee the stability and accuracy of the longitudinal motion of the FSHC under the lumped disturbances and actuator saturation.

$$\boldsymbol{u}(t) = \boldsymbol{u}_c(t) + \boldsymbol{u}_r(t) \quad (23)$$

where $\boldsymbol{u}_c(t)$ is the nominal control law, and $\boldsymbol{u}_r(t)$ is the control reaching law:

$$\begin{aligned}
\boldsymbol{u}_c(t) = -\boldsymbol{B}^{-1}\Big(&\mathrm{D}^{1-\alpha}\Big(\boldsymbol{S}^{+}\hat{K}(k_3\varepsilon - \|\boldsymbol{S}\| + \\
&2\|\boldsymbol{P}\|\|\boldsymbol{W}\| + \|\boldsymbol{S}^{\mathrm{T}}\|\|\mu\| + \lambda\|\boldsymbol{S}^{\mathrm{T}}\|\|\boldsymbol{g}\|)\Big) - \\
&\boldsymbol{B}^{-1}\left(\bar{\boldsymbol{f}}_1(\boldsymbol{x}_1,\boldsymbol{x}_2) + \bar{\boldsymbol{f}}_2(\boldsymbol{x}_1,\boldsymbol{x}_2) + \ddot{\boldsymbol{x}}_d + \hat{\boldsymbol{d}}_w\right) - \\
&\boldsymbol{B}^{-1}\left(\mathrm{D}^{1-\alpha}\left(\chi\dot{\boldsymbol{e}}_1(t) + \beta\frac{p}{q}\boldsymbol{e}_1(t)^{(p/q-1)}\dot{\boldsymbol{e}}_1(t)\right)\right) - \\
&\boldsymbol{B}^{-1}\left(\mathrm{D}^{1-\alpha}(\boldsymbol{S} - \boldsymbol{\varphi})\right)
\end{aligned} \quad (24)$$

$$\begin{aligned}
\boldsymbol{u}_r(t) = \boldsymbol{B}^{-1}\Big(&\mathrm{D}^{1-\alpha}\Big(-\boldsymbol{K}_1|\boldsymbol{S}|^m\mathrm{sgn}(\boldsymbol{S}) - \\
&\boldsymbol{K}_2|\boldsymbol{S}|^n\mathrm{sgn}(\boldsymbol{S}) - \hat{K}\tanh\left(\frac{\boldsymbol{S}}{\varepsilon}\right)\Big)\Big)
\end{aligned} \quad (25)$$

where $\boldsymbol{S}^{+} = \boldsymbol{S}(\boldsymbol{S}^{\mathrm{T}}\boldsymbol{S})^{-1}$ represents the pseudo-inverse of $\boldsymbol{S}$.

$\hat{K}$ represents the estimation of K and is updated by the adaptive law. $\tilde{K} = K - \hat{K}$ represents the estimation error, and the constants $\boldsymbol{P}$ and $\boldsymbol{g}$ are defined during the disturbance observer design. $\boldsymbol{W}$ is the upper bound of the lumped disturbance.

Lemma 4. For any $(x, y) \in R^2$, the Young's inequality is given as

$$xy \leqslant \frac{\bar{\beta}^a}{a}|x|^a + \frac{1}{b\bar{\beta}^b}|y|^b \tag{26}$$

Theorem 1. Considering the dynamic model of the FSHC in Equation (11), we design the AFONTSMC in Equation (23) with the disturbance observer in Equations (12) and (13) and the anti-windup compensator in Equation (18). If Assumptions 1 and 2 hold, the states of the system converge to the desired condition, and the system is globally asymptotically stable in finite time.

Proof. The AFONTSMC, enhanced by the disturbance observer, anti-windup compensation, and adaptive law, guarantees the stability of the FSHC. To validate the stability of the system, the Lyapunov function is designed as follows:

$$V_2 = \frac{1}{2}\boldsymbol{S}^{\mathrm{T}}\boldsymbol{S} + \frac{1}{2}\tilde{\boldsymbol{d}}_w^{\mathrm{T}}\boldsymbol{P}\tilde{\boldsymbol{d}}_w + \frac{1}{2}\tilde{K}^{\mathrm{T}}\tilde{K} + \frac{1}{2}\boldsymbol{\varphi}^{\mathrm{T}}\boldsymbol{\varphi} \tag{27}$$

By deriving (27), we obtain

$$\dot{V}_2 = \boldsymbol{S}^{\mathrm{T}}\dot{\boldsymbol{S}} + \tilde{\boldsymbol{d}}_w^{\mathrm{T}}\boldsymbol{P}\dot{\tilde{\boldsymbol{d}}}_w + \dot{\tilde{\boldsymbol{d}}}_w^{\mathrm{T}}\boldsymbol{P}\tilde{\boldsymbol{d}}_w + \tilde{K}^{\mathrm{T}}\dot{\tilde{K}} + \boldsymbol{\varphi}^{\mathrm{T}}\dot{\boldsymbol{\varphi}} \tag{28}$$

Substituting (20) into (28) yields

$$\begin{aligned}\dot{V}_2 = {} & \boldsymbol{S}^{\mathrm{T}}\left(\mathrm{D}^{\alpha-1}\left(\bar{\boldsymbol{f}}_1(\boldsymbol{x}_1,\boldsymbol{x}_2) + \bar{\boldsymbol{f}}_2(\boldsymbol{x}_1,\boldsymbol{x}_2) + \boldsymbol{B}\boldsymbol{\delta} + \boldsymbol{d}_w\right)\right) + \\ & \boldsymbol{S}^{\mathrm{T}}\left(\chi\dot{\boldsymbol{e}}_1(t) + \beta\frac{p}{q}\boldsymbol{e}_1(t)^{(p/q-1)}\dot{\boldsymbol{e}}_1(t) + \lambda\boldsymbol{g}\tilde{\boldsymbol{d}}_w\right) + \\ & \tilde{\boldsymbol{d}}_w^{\mathrm{T}}\boldsymbol{P}\dot{\tilde{\boldsymbol{d}}}_w + \dot{\tilde{\boldsymbol{d}}}_w^{\mathrm{T}}\boldsymbol{P}\tilde{\boldsymbol{d}}_w + \tilde{K}^{\mathrm{T}}\dot{\tilde{K}} + \boldsymbol{\varphi}^{T}\dot{\boldsymbol{\varphi}}\end{aligned} \tag{29}$$

Considering the actuator saturation $\Delta\boldsymbol{u} = \boldsymbol{\delta} - \boldsymbol{u}$, Equation (29) can be expressed as

$$\begin{aligned}\dot{V}_2 = {} & \boldsymbol{S}^{\mathrm{T}}\left(\mathrm{D}^{\alpha-1}\left(\bar{\boldsymbol{f}}_1(\boldsymbol{x}_1,\boldsymbol{x}_2) + \bar{\boldsymbol{f}}_2(\boldsymbol{x}_1,\boldsymbol{x}_2) + \boldsymbol{B}(\boldsymbol{u}+\Delta\boldsymbol{u}) + \boldsymbol{d}_w\right)\right) + \\ & \boldsymbol{S}^{\mathrm{T}}\left(\chi\dot{\boldsymbol{e}}_1(t) + \beta\frac{p}{q}\boldsymbol{e}_1(t)^{(p/q-1)}\dot{\boldsymbol{e}}_1(t) + \lambda\boldsymbol{g}\tilde{\boldsymbol{d}}_w\right) + \\ & \tilde{\boldsymbol{d}}_w^{\mathrm{T}}\boldsymbol{P}\dot{\tilde{\boldsymbol{d}}}_w + \dot{\tilde{\boldsymbol{d}}}_w^{\mathrm{T}}\boldsymbol{P}\tilde{\boldsymbol{d}}_w + \tilde{K}^{\mathrm{T}}\dot{\tilde{K}} + \boldsymbol{\varphi}^{T}\dot{\boldsymbol{\varphi}}\end{aligned} \tag{30}$$

By substituting Equations (23), (24), and (25) into (30), we obtain

$$\begin{aligned}\dot{V}_2 = {} & \boldsymbol{S}^{\mathrm{T}}(\mathrm{D}^{\alpha-1}(\bar{\boldsymbol{f}}_1(\boldsymbol{x}_1,\boldsymbol{x}_2) + \bar{\boldsymbol{f}}_2(\boldsymbol{x}_1,\boldsymbol{x}_2) + \boldsymbol{B}\Delta\boldsymbol{u}) + \boldsymbol{d}_w) + \\ & \boldsymbol{S}^{\mathrm{T}}\left\{\mathrm{D}^{\alpha-1}\boldsymbol{B}\left\{\boldsymbol{B}^{-1}(-\bar{\boldsymbol{f}}_1(\boldsymbol{x}_1,\boldsymbol{x}_2) - \bar{\boldsymbol{f}}_2(\boldsymbol{x}_1,\boldsymbol{x}_2) - \ddot{\boldsymbol{x}}_d - \hat{\boldsymbol{d}}_w)\right\}\right\} - \\ & \boldsymbol{S}^{\mathrm{T}}\left\{\mathrm{D}^{\alpha-1}\boldsymbol{B}\left(\boldsymbol{B}^{-1}\left(\mathrm{D}^{1-\alpha}\left(\boldsymbol{S}^{+}\hat{K}(k_3\varepsilon - \|\boldsymbol{S}\| + \right.\right.\right.\right. \\ & \left.\left.\left.\left.2\|\boldsymbol{P}\|\|\boldsymbol{W}\| + \|\boldsymbol{S}^{\mathrm{T}}\|\|\mu\| + \lambda\|\boldsymbol{S}^{\mathrm{T}}\|\|\boldsymbol{g}\|\right)\right)\right)\right\} - \\ & \boldsymbol{S}^{\mathrm{T}}\mathrm{D}^{\alpha-1}\boldsymbol{B}\left(\boldsymbol{B}^{-1}(\mathrm{D}^{1-\alpha}\left(\chi\dot{\boldsymbol{e}}_1(t) + \beta\frac{p}{q}\boldsymbol{e}_1(t)^{(p/q-1)}\dot{\boldsymbol{e}}_1(t)\right)\right) + \\ & \boldsymbol{S}^{\mathrm{T}}\mathrm{D}^{\alpha-1}\boldsymbol{B}\left(\boldsymbol{B}^{-1}\left(\mathrm{D}^{1-\alpha}\left(-\boldsymbol{K}_1|\boldsymbol{S}|^m\mathrm{sgn}(\boldsymbol{S}) - \right.\right.\right. \\ & \left.\left.\left.\boldsymbol{K}_2|\boldsymbol{S}|^n\mathrm{sgn}(\boldsymbol{S}) - \hat{K}\tanh\left(\frac{\boldsymbol{S}}{\varepsilon}\right)\right)\right)\right) + \\ & \boldsymbol{S}^{\mathrm{T}}\left[\chi\dot{\boldsymbol{e}}_1(t) + \beta\frac{p}{q}\boldsymbol{e}_1(t)^{(p/q-1)}\dot{\boldsymbol{e}}_1(t) + \lambda\boldsymbol{g}\tilde{\boldsymbol{d}}_w\right] - \\ & \boldsymbol{S}^{\mathrm{T}}\mathrm{D}^{\alpha-1}\boldsymbol{B}\left(\boldsymbol{B}^{-1}(\mathrm{D}^{1-\alpha}(\boldsymbol{S}-\boldsymbol{\varphi}))\right) + \tilde{\boldsymbol{d}}_w^{\mathrm{T}}\boldsymbol{P}\dot{\tilde{\boldsymbol{d}}}_w + \\ & \dot{\tilde{\boldsymbol{d}}}_w^{\mathrm{T}}\boldsymbol{P}\tilde{\boldsymbol{d}}_w + \tilde{K}^{\mathrm{T}}\dot{\tilde{K}} + \boldsymbol{\varphi}^{\mathrm{T}}\dot{\boldsymbol{\varphi}}\end{aligned} \tag{31}$$

From the proposed control law, the derivative of the Lyapunov function becomes

$$\begin{aligned}\dot{V}_2 = {} & \boldsymbol{S}^{\mathrm{T}}(\mathrm{D}^{\alpha-1}(\boldsymbol{B}\Delta\boldsymbol{u}) + \boldsymbol{d}_w) - \boldsymbol{S}^{\mathrm{T}}\left\{\mathrm{D}^{\alpha-1}(\hat{\boldsymbol{d}}_w)\right\} - \\ & \boldsymbol{S}^{\mathrm{T}}\left\{\left(\boldsymbol{S}^{+}\hat{K}(k_4\varepsilon - \|\boldsymbol{S}\| + 2\|\boldsymbol{P}\|\|\boldsymbol{W}\| + \right.\right. \\ & \left.\left.\|\boldsymbol{S}^{\mathrm{T}}\|\|\mu\| + \lambda\|\boldsymbol{S}^{\mathrm{T}}\|\|\boldsymbol{g}\|\right)\right\} + \boldsymbol{S}^{\mathrm{T}}\left(-\boldsymbol{K}_1|\boldsymbol{S}|^m\mathrm{sgn}(\boldsymbol{S}) - \right. \\ & \left.\boldsymbol{K}_2|\boldsymbol{S}|^n\mathrm{sgn}(\boldsymbol{S}) - \hat{K}\tanh\left(\frac{\boldsymbol{S}}{\varepsilon}\right)\right) + \boldsymbol{S}^{\mathrm{T}}\lambda\boldsymbol{g}\tilde{\boldsymbol{d}}_w - \\ & \boldsymbol{S}^{\mathrm{T}}(\boldsymbol{S}-\boldsymbol{\varphi}) + \tilde{\boldsymbol{d}}_w^{\mathrm{T}}\boldsymbol{P}\dot{\tilde{\boldsymbol{d}}}_w + \dot{\tilde{\boldsymbol{d}}}_w^{\mathrm{T}}\boldsymbol{P}\tilde{\boldsymbol{d}}_w + \tilde{K}^{\mathrm{T}}\dot{\tilde{K}} + \boldsymbol{\varphi}^{\mathrm{T}}\dot{\boldsymbol{\varphi}}\end{aligned} \tag{32}$$

Considering the stability demonstration of disturbance observer (14) and actuator saturation compensation of (18), we can deduce

$$\begin{aligned}\dot{V}_2 = {} & \boldsymbol{S}^{\mathrm{T}}\left(\mathrm{D}^{\alpha-1}(\boldsymbol{B}\Delta\boldsymbol{u}) + \boldsymbol{d}_w\right) - \boldsymbol{S}^{\mathrm{T}}\left\{\mathrm{D}^{\alpha-1}(\hat{\boldsymbol{d}}_w)\right\} - \\ & \boldsymbol{S}^{\mathrm{T}}\left\{\left(\boldsymbol{S}^{+}\hat{K}(k_4\varepsilon - \|\boldsymbol{S}\| + 2\|\boldsymbol{P}\|\|\boldsymbol{W}\| + \|\boldsymbol{S}^{\mathrm{T}}\|\|\mu\| + \right.\right. \\ & \left.\left.\lambda\|\boldsymbol{S}^{\mathrm{T}}\|\|\boldsymbol{g}\|\right)\right\} + \boldsymbol{S}^{\mathrm{T}}\left(-\boldsymbol{K}_1|\boldsymbol{S}|^m\mathrm{sgn}(\boldsymbol{S}) - \right. \\ & \left.\boldsymbol{K}_2|\boldsymbol{S}|^n\mathrm{sgn}(\boldsymbol{S}) - \hat{K}\tanh\left(\frac{\boldsymbol{S}}{\varepsilon}\right)\right) + \\ & \boldsymbol{S}^{\mathrm{T}}\lambda\boldsymbol{g}\tilde{\boldsymbol{d}}_w - \boldsymbol{S}^{\mathrm{T}}(\boldsymbol{S}-\boldsymbol{\varphi}) + \tilde{K}^{\mathrm{T}}\tilde{K} + \\ & \tilde{\boldsymbol{d}}_w^{\mathrm{T}}\boldsymbol{P}\left(\dot{\boldsymbol{d}}_w - \boldsymbol{g}\tilde{\boldsymbol{d}}_w\right) + \left(\dot{\boldsymbol{d}}_w - \boldsymbol{g}\tilde{\boldsymbol{d}}_w\right)^{\mathrm{T}}\boldsymbol{P}\tilde{\boldsymbol{d}}_w + \\ & \boldsymbol{\varphi}^{\mathrm{T}}\left(-k_3\boldsymbol{\varphi} - \frac{\left\|\boldsymbol{S}^{\mathrm{T}}\mathrm{D}^{\alpha-1}(\boldsymbol{B}\Delta\boldsymbol{u})\right\| + 1/2\rho^2(\Delta\boldsymbol{u})^{\mathrm{T}}\Delta\boldsymbol{u}}{\|\boldsymbol{\varphi}\|^2}\boldsymbol{\varphi} + \rho\Delta\boldsymbol{u}\right)\end{aligned} \tag{33}$$

We design the adaptive law for estimating adjustable gain $\hat{K}$ as

$$\dot{\hat{K}} = 2\|\boldsymbol{P}\|\|\boldsymbol{W}\| + \|\boldsymbol{S}^{\mathrm{T}}\|\|\mu\| + \lambda\|\boldsymbol{S}^{\mathrm{T}}\|\|\boldsymbol{g}\| \tag{34}$$

By using the Lemma 3 and substituting Equation (34) into (33), we derive

$$\begin{aligned}\dot{V}_2 \leqslant\ & \boldsymbol{S}^{\mathrm{T}}\left(\mathrm{D}^{\alpha-1}(\boldsymbol{B}\Delta\boldsymbol{u}) + \boldsymbol{d}_w\right) - \boldsymbol{S}^{\mathrm{T}}\left\{\mathrm{D}^{\alpha-1}(\hat{\boldsymbol{d}}_w)\right\} - \\ & \boldsymbol{S}^{\mathrm{T}}\left\{\left(\boldsymbol{S}^{+}\hat{K}\left(k_4\varepsilon - \|\boldsymbol{S}\| + 2\|\boldsymbol{P}\|\|\boldsymbol{W}\| + \|\boldsymbol{S}^{\mathrm{T}}\|\|\mu\| + \right.\right.\right. \\ & \left.\left.\left.\lambda\|\boldsymbol{S}^{\mathrm{T}}\|\|\boldsymbol{g}\|\right)\right\} + \boldsymbol{S}^{\mathrm{T}}\left(-\boldsymbol{K}_1|\boldsymbol{S}|^{m}\mathrm{sgn}(\boldsymbol{S}) - \right. \\ & \left.\boldsymbol{K}_2|\boldsymbol{S}|^{n}\mathrm{sgn}(\boldsymbol{S})\right) + \hat{K}\left(k_4\varepsilon - \|\boldsymbol{S}\|\right) + \boldsymbol{S}^{\mathrm{T}}\lambda\boldsymbol{g}\tilde{\boldsymbol{d}}_w - \\ & \boldsymbol{S}^{\mathrm{T}}(\boldsymbol{S}-\boldsymbol{\varphi}) - \tilde{\boldsymbol{d}}_w^{\mathrm{T}}\boldsymbol{Q}\tilde{\boldsymbol{d}}_w + 2\tilde{\boldsymbol{d}}_w^{\mathrm{T}}\boldsymbol{P}\dot{\boldsymbol{d}}_w - \\ & \tilde{K}^{\mathrm{T}}\left(2\|\boldsymbol{P}\|\|\boldsymbol{W}\| + \|\boldsymbol{S}^{\mathrm{T}}\|\|\mu\| + \lambda\|\boldsymbol{S}^{\mathrm{T}}\|\|\boldsymbol{g}\|\right) - \\ & k_3\boldsymbol{\varphi}^{\mathrm{T}}\boldsymbol{\varphi} - \|\boldsymbol{S}^{\mathrm{T}}\mathrm{D}^{\alpha-1}(\boldsymbol{B}\Delta\boldsymbol{u})\| - 1/2\rho^2(\Delta\boldsymbol{u})^{\mathrm{T}}\Delta\boldsymbol{u} + \boldsymbol{\varphi}^{\mathrm{T}}\rho\Delta\boldsymbol{u}\end{aligned} \tag{35}$$

where K is the parameter and $\dot{K} = 0$ such that $\dot{\hat{K}} = -\dot{\tilde{K}}$, $k_4 = 0.278\,5$, and $\varepsilon > 0$. Considering Lemma 4 and $\lambda_{\min}(\boldsymbol{Q})\|\tilde{\boldsymbol{d}}_w\|^2 \leqslant \tilde{\boldsymbol{d}}_w^{\mathrm{T}}\boldsymbol{Q}\tilde{\boldsymbol{d}}_w \leqslant \lambda_{\max}(\boldsymbol{Q})\|\tilde{\boldsymbol{d}}_w\|^2$, the equation is given as

$$\begin{aligned}\dot{V}_2 \leqslant\ & \|\boldsymbol{S}^{\mathrm{T}}(\mathrm{D}^{\alpha-1}(\boldsymbol{B}\Delta\boldsymbol{u})\| + \boldsymbol{S}^{\mathrm{T}}\left\{\mathrm{D}^{\alpha-1}(\hat{\boldsymbol{d}}_w)\right\} - \\ & \hat{K}(2\|\boldsymbol{P}\|\|\boldsymbol{W}\| + \|\boldsymbol{S}^{\mathrm{T}}\|\|\mu\| + \lambda\|\boldsymbol{S}^{\mathrm{T}}\|\|\boldsymbol{g}\|) - \\ & \boldsymbol{K}_1|\boldsymbol{S}|^{m+1} - \boldsymbol{K}_2|\boldsymbol{S}|^{n+1} - \boldsymbol{S}^{\mathrm{T}}(\boldsymbol{S}-\boldsymbol{\varphi}) - \\ & \tilde{K}^{\mathrm{T}}(2\|\boldsymbol{P}\|\|\boldsymbol{W}\| + \|\boldsymbol{S}^{\mathrm{T}}\|\|\mu\| + \lambda\|\boldsymbol{S}^{\mathrm{T}}\|\|\boldsymbol{g}\|) + \\ & \boldsymbol{S}^{\mathrm{T}}\lambda\boldsymbol{g}\tilde{\boldsymbol{d}}_w + 2\|\tilde{\boldsymbol{d}}_w\|\|\boldsymbol{P}\|\|\boldsymbol{W}\| - \lambda_{\min}(\boldsymbol{Q})\|\tilde{\boldsymbol{d}}_w\|^2 - \\ & k_3\boldsymbol{\varphi}^{\mathrm{T}}\boldsymbol{\varphi} - \|\boldsymbol{S}^{\mathrm{T}}\mathrm{D}^{\alpha-1}(\boldsymbol{B}\Delta\boldsymbol{u})\| - 1/2\rho^2(\Delta\boldsymbol{u})^{\mathrm{T}}\Delta\boldsymbol{u} + \\ & \varphi^{\mathrm{T}}\rho\Delta\boldsymbol{u} \leqslant \|\boldsymbol{S}^{\mathrm{T}}(\mathrm{D}^{\alpha-1}(\boldsymbol{B}\Delta\boldsymbol{u})\| + \|\boldsymbol{S}^{\mathrm{T}}\|\|\mathrm{D}^{\alpha-1}(\tilde{\boldsymbol{d}}_w)\| - \\ & \hat{K}(2\|\boldsymbol{P}\|\|\boldsymbol{W}\| + \|\boldsymbol{S}^{T}\|\|\mu\| + \lambda\|\boldsymbol{S}^{\mathrm{T}}\|\|\boldsymbol{g}\|) - \\ & \lambda_{\min}(\boldsymbol{K}_1)|\boldsymbol{S}|^{m+1} - \lambda_{\min}(\boldsymbol{K}_2)|\boldsymbol{S}|^{n+1} - \\ & \tilde{K}^{\mathrm{T}}(2\|\boldsymbol{P}\|\|\boldsymbol{W}\| + \|\boldsymbol{S}^{\mathrm{T}}\|\|\mu\| + \lambda\|\boldsymbol{S}^{\mathrm{T}}\|\|\boldsymbol{g}\|) + \\ & \|\boldsymbol{S}^{\mathrm{T}}\|\lambda g\|\tilde{\boldsymbol{d}}_w\| + 2\|\tilde{\boldsymbol{d}}_w\|\|\boldsymbol{P}\|\|\boldsymbol{W}\| - \lambda_{\min}(\boldsymbol{Q})\|\tilde{\boldsymbol{d}}_w\|^2 - \\ & k_3\boldsymbol{\varphi}^{\mathrm{T}}\boldsymbol{\varphi} - \boldsymbol{S}^{\mathrm{T}}\boldsymbol{S} + \frac{1}{2}\boldsymbol{S}^{\mathrm{T}}\boldsymbol{S} + \frac{1}{2}\boldsymbol{\varphi}^{\mathrm{T}}\boldsymbol{\varphi} - \\ & \|\boldsymbol{S}^{\mathrm{T}}\mathrm{D}^{\alpha-1}(\boldsymbol{B}\Delta\boldsymbol{u})\| - \frac{1}{2}\rho^2(\Delta\boldsymbol{u})^{\mathrm{T}}\Delta\boldsymbol{u} + \frac{1}{2}\boldsymbol{\varphi}^{\mathrm{T}}\boldsymbol{\varphi} + \\ & \frac{1}{2}\rho^2(\Delta\boldsymbol{u})^{\mathrm{T}}\Delta\boldsymbol{u}\end{aligned} \tag{36}$$

Supposing that $K \geqslant \|\tilde{\boldsymbol{d}}_w\|$ and considering Lemma 1 for any $\|\mathrm{D}^{\alpha-1}(\tilde{\boldsymbol{d}}_w)\| \leqslant \mu\|\tilde{\boldsymbol{d}}_w\|$, we can deduce

$$\begin{aligned}\dot{V}_2 \leqslant\ & -\hat{K}(2\|\boldsymbol{P}\|\|\boldsymbol{W}\| + \|\boldsymbol{S}^{\mathrm{T}}\|\|\mu\| + \|\boldsymbol{S}^{\mathrm{T}}\|k) - \\ & \lambda_{\min}(\boldsymbol{K}_1)|\boldsymbol{S}|^{m+1} - \lambda_{\min}(\boldsymbol{K}_2)|\boldsymbol{S}|^{n+1} - \\ & \lambda_{\min}(\boldsymbol{Q})\|\tilde{\boldsymbol{d}}_w\|^2 - \frac{1}{2}\boldsymbol{S}^{\mathrm{T}}\boldsymbol{S} + (1-k_3)\boldsymbol{\varphi}^{\mathrm{T}}\boldsymbol{\varphi} - \\ & \tilde{K}^{\mathrm{T}}\left(2\|\boldsymbol{P}\|\|\boldsymbol{W}\| + \|\boldsymbol{S}^{\mathrm{T}}\|\|\mu\| + \lambda\|\boldsymbol{S}^{\mathrm{T}}\|\|\boldsymbol{g}\|\right) + \\ & K\left(\|\boldsymbol{S}^{\mathrm{T}}\|\mu + \|\boldsymbol{S}^{\mathrm{T}}\|\lambda\boldsymbol{g} + 2\|\boldsymbol{P}\|\|\boldsymbol{W}\|\right) \leqslant \\ & -\lambda_{\min}(\boldsymbol{K}_1)|\boldsymbol{S}|^{m+1} - \lambda_{\min}(\boldsymbol{K}_2)|\boldsymbol{S}|^{n+1} - \\ & \frac{1}{2}\boldsymbol{S}^{\mathrm{T}}\boldsymbol{S} - \lambda_{\min}(\boldsymbol{Q})\|\tilde{\boldsymbol{d}}_w\|^2 + (1-k_3)\boldsymbol{\varphi}^{\mathrm{T}}\boldsymbol{\varphi}\end{aligned} \tag{37}$$

We select $k_3 > 1$, then $\dot{V}_2 \leqslant 0$.

Thus, the closed system of the FSHC with the AFONTSMC strategy, which considers the disturbance observer, saturation compensation, and parameter adaptive law, is globally asymptotically stable.

Remark 3. By incorporating the adaptive fractional-order nonsingular fast terminal sliding mode surface with disturbance observer, as described in Equations (14) and (15) and the anti-windup compensator in Equation (20), the closed system is globally asymptotically stable. In this work, the adaptive fractional-order nonsingular fast terminal sliding mode surface, combined with a nonlinear disturbance observer, is developed to mitigate the adverse effects of lumped disturbances. The designed controller only requires to exceed the disturbance observer error. The reaching law of the SMC is enhanced by the continuous hyperbolic tangent function with adaptive law, significantly reducing chattering. The anti-windup compensator is designed with fractional-order items for the actuator saturation, considering the dynamic model of the FSHC and actuator deviation. This approach minimizes the influence of the actuator saturation on system performance.

4 Simulation results

Matlab/Simulink simulations are conducted to demonstrate the applicability and efficiency of the proposed controller. The enhanced AFONTSMC with disturbance observer and saturation compensation is applied to the FSHC. The parameters of the FSHC are selected as follows: $m = 2.62 \times 10^5$ kg, $I_y = 3.9 \times 10^5$ kg·m^2, $U_e = 22.9$ m/s, $L_s = 17.86$ m, $a_1 = 6.06\,(1/\mathrm{s})$, $a_2 = 0.338\,(1/\mathrm{s}^2)$, $a_3 = 3.14$ m, $a_4 = 42.4\,(\mathrm{m/s})$, $a_5 = 454\,(\mathrm{m/s}^2)$, $a_6 = 51.5\,(\mathrm{m/s}^2)$, $a_7 = 62.9$ m/s^2, $b_1 = 0.016\,(1/\mathrm{m})$, $b_3 = 0.069\,(1/(\mathrm{m}\cdot\mathrm{s}^2))$, $b_4 = 8.45\,(1/\mathrm{s})$, $b_5 = 0.654\,(1/\mathrm{s}^2)$, and $b_6 = -4.58\,(1/\mathrm{s}^2)$ (Liu et al., 2019b).

Comparative experiments are conducted in the following two scenarios. Scenario 1 assesses the efficiency of the proposed nonlinear disturbance observer with fractional-order calculus. Simulations for FSHC's longitudinal motion

control are carried out under various conditions. Scenario 2 presents comparative simulations of the full-order fast terminal SMC (TSMC), FOTSMC without saturation compensation, and the enhanced AFONTSMC.

4.1 Disturbance observer simulation

The system uncertainty $\Delta \boldsymbol{f}_1(\boldsymbol{x}_1, \boldsymbol{x}_2), \Delta \boldsymbol{f}_2(\boldsymbol{x}_1, \boldsymbol{x}_2)$ contains unmodeled dynamics and parameter perturbations, which typically fall within a range of approximately ±10% of the nominal values. $\boldsymbol{d}_w = \Delta \boldsymbol{f}_1(\boldsymbol{x}_1, \boldsymbol{x}_2) + \Delta \boldsymbol{f}_2(\boldsymbol{x}_1, \boldsymbol{x}_2) + \boldsymbol{d}_1$ is the lumped disturbance and $\boldsymbol{d}_1$ is the external disturbance. For the analysis of the ocean wave and external disturbance, readers can refer to Liu et al. (2019b). A significant wave height of 1.5 m and a wave encounter angle of 60° are chosen for the simulations. The angles of the aft and fore foils are limited at ±45°.

The disturbance observer is designed to estimate the force and moment of lumped disturbance. The parameters of the disturbance observer are determined as $\lambda_1 = 0.1$ and $\lambda_2 = 0.2$. The performance of the observer is significantly influenced by $\boldsymbol{g}$; therefore, this parameter is carefully selected through trial and error, and the RMSE of different parameters is compared in Table 2. The RMSE and error mean are defined as follows:

$$E_{\mathrm{RMSE}} = \sqrt{\frac{1}{N}\sum_{i=1}^{N}\left|E(i)\right|^2}, E_{\mathrm{avg}} = \frac{1}{N}\sum_{i=1}^{N}\left|E(i)\right| \quad (38)$$

Table 2 RMSE of different parameters of disturbance observer

Parameter of $\boldsymbol{g}$	RMSE of disturbance force	RMSE of disturbance moment
[2 0; 0 12]	0.806 1	0.166 6
[5 0; 0 12]	0.383 4	0.164 2
[10 0; 0 12]	0.185 8	0.158 6
[15 0; 0 12]	0.211 4	0.168 2
[18 0; 0 12]	0.238 1	0.159 4
[10 0; 0 5]	0.494 7	0.269 9
[10 0; 0 9]	0.230 2	0.189 9
[10 0; 0 15]	0.192 5	0.167 7

The comparation results in Table 2 suggest that $\boldsymbol{g}$ = [10 0 ; 0 12] is the optimal selection for the disturbance observer because it yields the minimal RMSE when adjusting g_1 and g_2. Thus, $\boldsymbol{g}$ = [10 0 ; 0 12] is selected as the parameter for the disturbance design. The fractional parameter of disturbance observer is selected as $\alpha = 0.5$. To show the effectiveness of the nonlinear disturbance observer proposed, the nominal nonlinear disturbance observer (DOB) and the disturbance observer incorporating fractional-order calculus (FNDOB) proposed in this paper are compared (Figures 4–6). The simulations of the actual lumped disturbance, DOB, and FNDOB are shown in Figures 3 and 4. The estimation errors of the DOB and FNDOB of the lumped disturbance force and moment are evaluated in Figures 5 and 6, respectively.

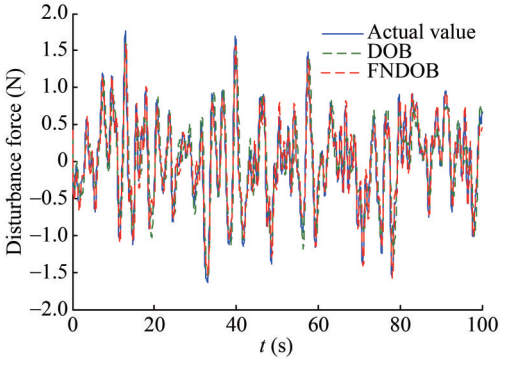

Figure 3 Disturbance force of the FSHC

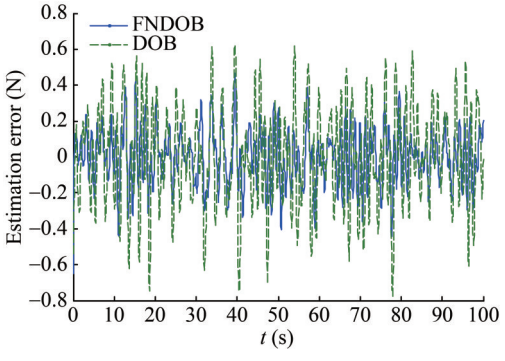

Figure 4 Estimation error of disturbance force

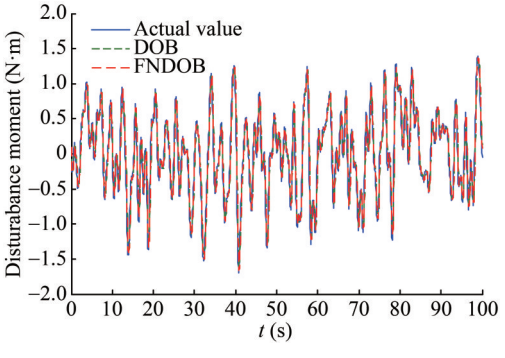

Figure 5 Disturbance moment of the FSHC

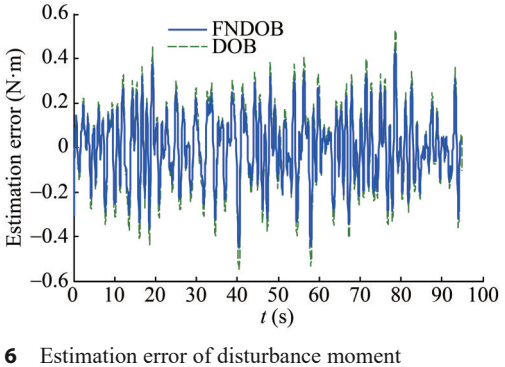

Figure 6 Estimation error of disturbance moment

Figures 3–6 show that the FNDOB performs better than the DOB in that the estimation error of the FNDOB is less than that of the DOB. Thus, the proposed nonlinear disturbance observer incorporating fractional-order calculus performs exceptionally in accurately estimating lumped disturbances. The estimation error remains bounded and ultimately converges to a sufficiently small value. The proposed nonlinear disturbance observer is effective for disturbance estimation with reduced conservation.

4.2 Simulation of the proposed controller

To demonstrate the performance of the controller, comparative simulations among TSMC, FOTSMC, and AFONTSMC are conducted in Figures 7–10. The control performance of heave motion is depicted in Figures 7 and 8, whereas the pitch angle is illustrated in Figures 9 and 10. The control angle of the AFONTSMC and TSMC are presented in Figures 11 and 12. The parameters selected for the proposed controller are $\boldsymbol{P} = [1/36 \;\; 0\,;\, 0 \;\; 1/18]$, $\boldsymbol{K}_2 = [0.01 \;\; 0\,;\, 0 \;\; 0.01]$, $m = 0.5$, $n = 1.2$, $k_3 = 3$, $\rho = 10$, and $\alpha = 0.6$.

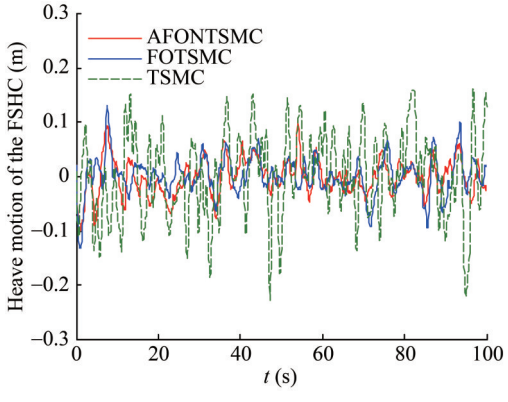

Figure 7 Heave motion of the FSHC

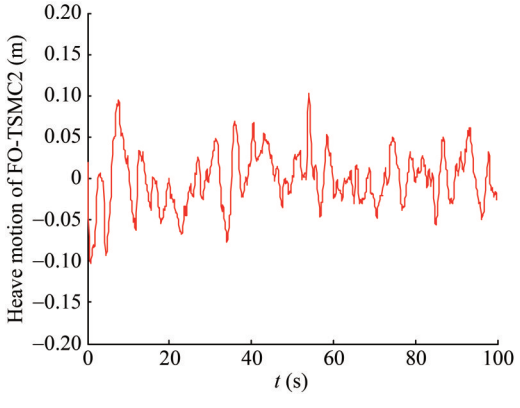

Figure 8 Heave motion of AFONTSMC

To comprehensively assess the efficacy of the three distinct controllers, we establish a set of specific performance criteria, incorporating RMSE and steady-state error mean

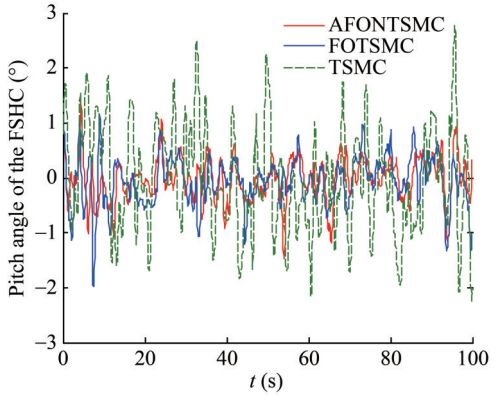

Figure 9 Pitch angle of the FSHC

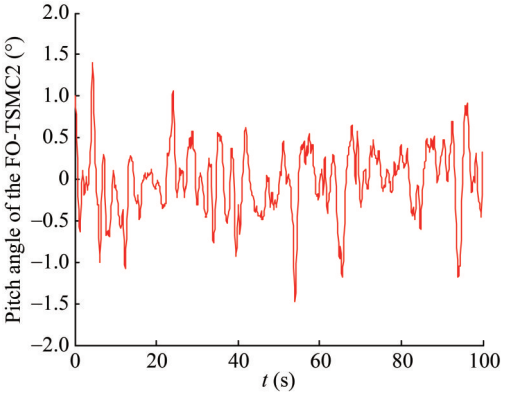

Figure 10 Pitch angle of the AFONTSMC

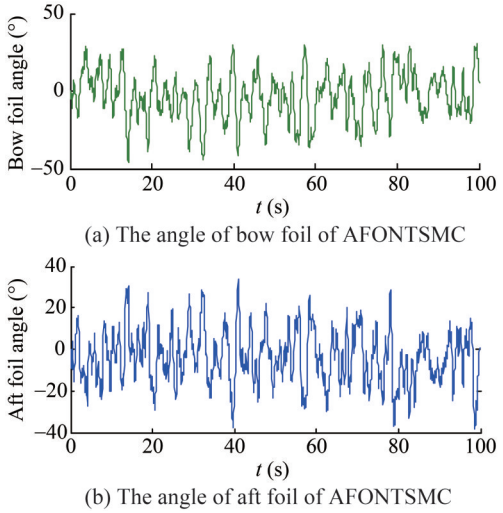

Figure 11 Control angle of the AFONTSMC

values. The desired equilibrium for heave motion and pitch angle is set to zero. Subsequently, RMSE values for heave motion are computed, as depicted in Figure 12, whereas Figure 13 illustrates the corresponding RMSE values for pitch angle. Tables 3–6 display the RMSE values and mean errors for heave motion and pitch angle at various encounter angles (30°, 60°, 90°, 120°, and 150°).

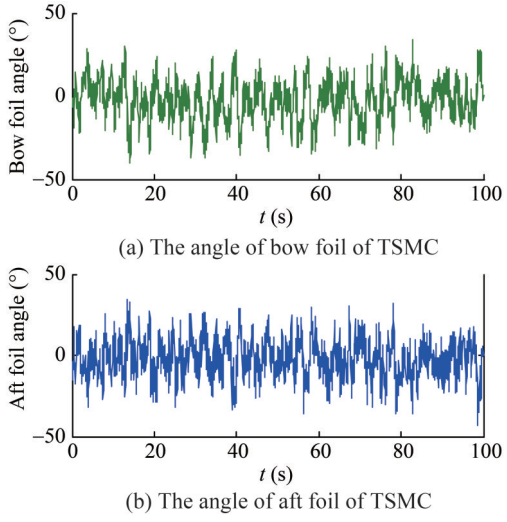

(a) The angle of bow foil of TSMC

(b) The angle of aft foil of TSMC

Figure 12 Control angle of the TSMC

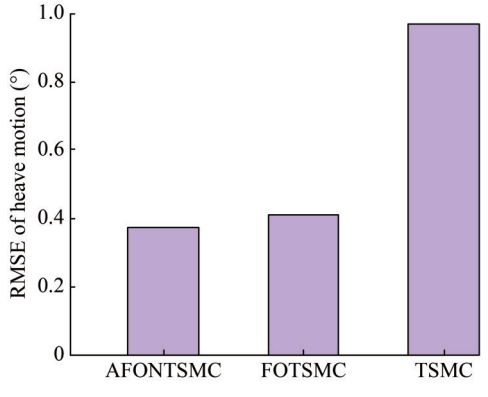

Figure 13 RMSE of heave motion of the FSHC

Figures 7–10, 13, and 14 and Tables 2–5 indicate that the RMSE and mean error metrics associated with the proposed controller AFONTSMC surpass those of TSMC. The precision achieved by AFONTSMC is approximately threefold greater than that by TSMC. The adeptness of AFONTSMC in mitigating system disturbances is evidenced by its capability to significantly reduce stability errors. Moreover, the results in Tables 2–5 underscore the consistent precision of the proposed controller across various encounter angles, thereby highlighting its efficacy in handling lumped disturbances. Figures 11 and 12 illustrate the markedly smoother performance of AFONTSMC compared with TSMC. The integration of fractional-order SMC with disturbance observation and adaptive fast-reaching law augmented by hyperbolic tangent functions is effective in attenuating disturbance effects and controller chattering. Additionally, AFONTSMC outperforms FOTSMC because of its proficient saturation compensation mechanism, which effectively manages actuator saturation. Consequently, the controller presented in this work exhibits higher steady-state performance and reduced conservation in the face of lumped disturbances and actuator saturation.

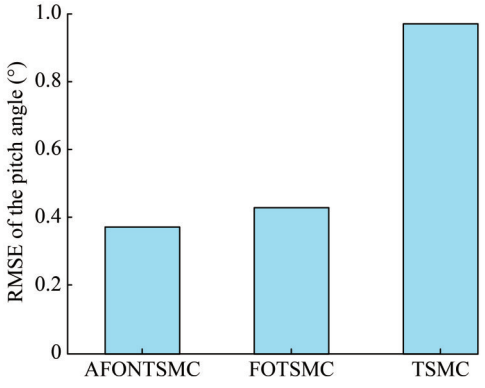

Figure 14 RMSE of the pitch angle of the FSHC

Table 3 RMSE of heave motion

Control method	Encounter angle				
	30°	60°	90°	120°	150°
FO-TSMC2	0.038	0.032	0.041	0.029	0.036
FO-TSMC	0.042	0.035	0.048	0.035	0.038
TSMC	0.053	0.076	0.066	0.071	0.068

Table 4 Error mean of heave motion

Control method	Encounter angle				
	30°	60°	90°	120°	150°
FO-TSMC2	0.033	0.025	0.033	0.023	0.028
FO-TSMC	0.036	0.028	0.037	0.027	0.031
TSMC	0.056	0.063	0.054	0.056	0.054

Table 5 RMSE of pitch angle

Control method	Encounter angle				
	30°	60°	90°	120°	150°
FO-TSMC2	0.283	0.372	0.337	0.351	0.380
FO-TSMC	0.307	0.428	0.349	0.372	0.392
TSMC	0.551	0.935	0.620	0.788	0.901

Table 6 Error mean of pitch angle

Control method	Encounter angle				
	30°	60°	90°	120°	150°
FO-TSMC2	0.207	0.295	0.259	0.262	0.290
FO-TSMC	0.232	0.316	0.267	0.288	0.319
TSMC	0.415	0.785	0.509	0.691	0.719

Furthermore, while the FSHC cruises in the sea, the wave height undergoes regular fluctuations. The sailing height of the FSHC must adjust accordingly to maintain stability. Two distinct conditions for desired sailing heights are established to demonstrate the tracking capabilities of the controllers: case 1: $x_{z1} = 0.1 \times \tanh((t - 30)/0.1)$, and case 2: $x_{z2} = 0.1 \times \tanh((t - 50)/0.1)$. The

tracking performance of AFONTSMC, FOTSMC, and TSMC are compared in Figures 15 and 16.

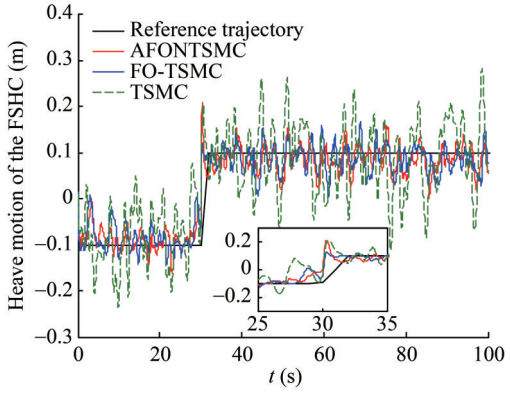

Figure 15 The tracking performance of case 1

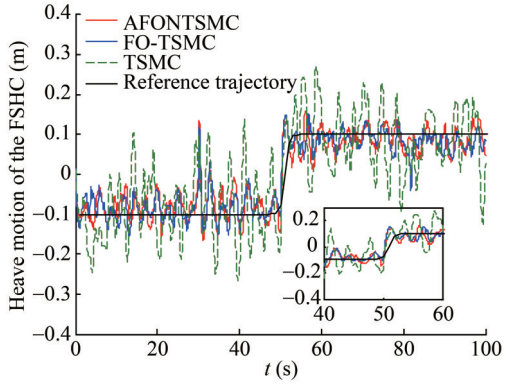

Figure 16 The tracking performance of case 2

In Figure 15, the convergence times of AFONTSMC, FOTSMC, and TSMC are recorded as 2.6, 2.9, and 3.2 s, respectively. In Figure 16, these convergence times are slightly adjusted to 2.8, 3.1, and 3.3 s. The proposed methodology exhibits a rapid transient procedure with significantly enhanced trajectory tracking accuracy during the transient phase. This performance superiority over TSMC underscores the effectiveness of the proposed method. Moreover, its steady-state error is significantly diminished compared with that of TSMC during height tracking. These results collectively indicate that the proposed controller not only delivers outstanding steady-state performance but also excels in transient trajectory tracking capabilities.

5 Conclusions

This study introduces an enhanced AFONTSMC tailored for longitudinal motion control of the FSHC in the presence of lumped disturbances, model uncertainties, and actuator saturation. A nonlinear disturbance observer utilizing fractional-order calculus is devised for the accurate estimation of lumped disturbances. The fractional-order nonsingular SMC is augmented by incorporating disturbance estimation, and the adaptive fast-reaching law of the controller is refined using the hyperbolic tangent function. An anti-windup compensator is also devised to mitigate the effects of actuator saturation. Simulations are conducted to compare the performance of AFONTSMC against FOTSMC and TSMC in longitudinal motion and desired height tracking. The results indicate that the proposed controller achieves a faster convergence rate and higher control accuracy, exhibiting reduced controller chattering and conservativeness under disturbances and actuator saturation. The proposed controller demonstrates effectiveness in FSHC control.

Funding Supported by Natural Science Basic Research Program of Shaanxi under Grant No. 2023-JC-QN-0751, No. 2023-JC-QN-0778; Fundamental Research Funds for the Central Universities, CHD under Grant No. 300102324102; the National Natural Science Foundation of China under Grant Nos. 72471035, 52271313; Fundamental Research Funds for the Central Universities under Grant No. XK2040021004025.

Competing interest The authors have no competing interests to declare that are relevant to the content of this article.

References

Alipour M, Malekzadeh M, Ariaei A (2022) Practical fractional-order nonsingular terminal sliding mode control of spacecraft. ISA Transactions 128: 162-173. DOI:10.1016/j.isatra.2021.10.022

Chak YC, Varatharajoo R, Razoumny Y (2017) Disturbance observer-based fuzzy control for flexible spacecraft combined attitude & sun tracking system. Acta Astronautica 133: 302-310. DOI:10.1016/j.actaastro.2016.12.028

Chen M, Ge SS, Choo YS (2009) Neural network tracking control of ocean surface vessels with input saturation. IEEE International Conference on Automation and Logistics (ICAL), Shenyang, China, 85-89. DOI:10.1109/ICAL.2009.5262972

Chen M, Ge SS, Ren BB (2011) Adaptive tracking control of uncertain MIMO nonlinear systems with input constraints. Automatica 47(3): 452-465. DOI:10.1016/j.automatica.2011.01.025

Deng YJ, Zhang XK, Im N, Liang CL (2020) Compound learning tracking control of a switched fully-submerged hydrofoil craft. Ocean Engineering 219: 108260. DOI:10.1016/j.oceaneng.2020.108260

Elmokadem T, Zribi M, Youcef-Toumi K (2016) Terminal sliding mode control for the trajectory tracking of underactuated autonomous underwater vehicles. Ocean Engineering 129: 613-625. DOI:10.1016/j.oceaneng.2016.10.032

Fossen TI (1994) Guidance and control of ocean vehicles. Wiley, New York, USA

He HK, Wang N, Huang DZ, Han B (2024) Active vision-based finite-time trajectory-tracking control of an unmanned surface vehicle without direct position measurements. IEEE Transactions on Intelligent Transportation Systems 25(9): 12151-12162. DOI:10.1109/TITS.2024.3364770

Hu CD, Wu DF, Liao YX, Hu X (2021) Sliding mode control unified with the uncertainty and disturbance estimator for dynamically

positioned vessels subjected to uncertainties and unknown disturbances. Applied Ocean Research 109: 102564. DOI:10.1016/j.apor.2021.102564

Hu TS, Lin ZL, Chen BM (2002) An analysis and design method for linear systems subject to actuator saturation and disturbance. Automatica 38(2): 351-359. DOI:10.1016/S0005-1098(01)00209-6

Hua CC, Chen JN, Guan XP (2019) Fractional-order sliding mode control of uncertain QUAVs with time-varying state constraints. Nonlinear Dynamics 95(2): 1347-1360. DOI: 10.1007/s11071-018-4632-0

Ionescu C, Muresan C (2015) Sliding mode control for a class of subsystems with fractional order varying trajectory dynamics. Fractional Calculus and Applied Analysis 18(6): 1441-1451. DOI: 10.1515/fca-2015-0083

Ionescu CM, Dulf EH, Ghita M, Muresan CI (2020) Robust controller design: Recent emerging concepts for control of mechatronic systems. Journal of the Franklin Institute-Engineering and Applied Mathematics 357(12): 7818-7844. DOI: 10.1016/j.jfranklin.2020.05.046

Kim SH, Yamato H (2002) A study on longitudinal control system for fully-submerged hydrofoil based on optimal preview servo system. Proceedings of ISOPE Pacific/Asia Offshore Mechanics Symposium, Daejeon, Korea, 159-164

Kim SH, Yamato H (2004) An experimental study of the longitudinal motion control of a fully submerged hydrofoil model in following seas. Ocean Engineering 31(5): 523-537. DOI:10.1016/j.oceaneng.2003.10.003

Labbadi M, Defoort M, Incremona GP, Djemai M (2023) Fractional-order integral terminal sliding-mode control for perturbed nonlinear systems with application to quadrotors. International Journal of Robust and Nonlinear Control 33(17): 10278-10303. DOI:10.1002/rnc.6608

Li HY, Yu JY, Hilton C, Liu HH (2013) Adaptive sliding-mode control for nonlinear active suspension vehicle systems using T–S fuzzy approach. IEEE Transactions on Industrial Electronics 60(8): 3328-3338. DOI:10.1109/TIE.2012.2202354

Li WH, Sun YQ, Chen HQ, Wang G (2016) Model predictive controller design for ship dynamic positioning system based on state-space equations. Journal of Marine Science & Technology 22(3): 426-431. DOI:10.1007/s00773-016-0425-7

Liu HD, Fu YX, Li B (2022) Study of the LQRY-SMC control method for the longitudinal motion of fully submerged hydrofoil crafts. Journal of Marine Science and Engineering 10(10): 1390. DOI:10.3390/jmse10101390

Liu S, Niu HM, Zhang LY, Guo XJ (2019a) Adaptive compound second order terminal sliding mode control for the longitudinal attitude control of the fully submerged hydrofoil vessel. Advances in Mechanical Engineering 12: 1-13. DOI: 10.1177/1687814019895637

Liu S, Niu HM, Zhang LY, Xu CK (2019b) Modified adaptive complementary sliding mode control for the longitudinal motion stabilization of the fully-submerged hydrofoil craft. International Journal of Naval Architecture and Ocean Engineering 11(1): 584-596. DOI:10.1016/j.ijnaoe.2018.10.003

Liu S, Xu CK, Zhang LY (2017) Robust course keeping control of a fully submerged hydrofoil vessel with actuator dynamics: A singular perturbation approach. Mathematical Problems in Engineering 2017: 1-14. DOI:10.1155/2017/6402012

Lungu MH (2020) Control of double gimbal control moment gyro systems using the backstepping control method and a nonlinear disturbance observer. Acta Astronautica 180: 639-649. DOI: 10.1016/j.actaastro.2020.10.040

Melicio R, Mendes VMF, Catalao JPS (2010) Fractional-order control and simulation of wind energy systems with PMSG/full-power converter topology. Energy Conversion & Management 51(6): 1250-1258. DOI:10.1016/j.enconman.2009.12.036

Mohammadi A, Tavakoli M, Marquez HJ, Hashemzadeh F (2013) Nonlinear disturbance observer design for robotic manipulators. Control Engineering Practice 21(3): 253-267. DOI: 10.1016/J.CONENGPRAC.2012.10.008

Mujumdar A, Tamhane B, Kurode S (2015) Observer-based sliding mode control for a class of noncommensurate fractional-order systems. IEEE/ASME Transactions on Mechatronics 20(5): 2504-2512. DOI10.1109/TMECH.2014.2386914

Ni JK, Liu L, Liu CX, Hu XY (2017) Fractional order fixed-time nonsingular terminal sliding mode synchronization and control of fractional order chaotic systems. Nonlinear Dynamics 89(3): 2065-2083

Niu HM, Liu S (2024) Combined cubature kalman and smooth variable structure filtering based on multi-kernel maximum correntropy criterion for the fully submerged hydrofoil craft. Applied Sciences-Basel. 14(9): DOI:10.3390/app14093952

Ren JS, Yang YS (2005) Controller design of hydrofoil catamaran with dynamical output-feedback H_∞ scheme. Journal of Traffic and Transportation Engineering 5(1): 45-48

Ren JS, Yang YS, Zheng YF, Li TS (2005) Fuzzy model-based robust controller design for hydrofoil catamaran. American Control Conference 2005: 4339-4344

Saqib NU, Rehan M, Hussain M, Zheng ZW (2019) Observer-based anti-windup compensator design for nonlinear systems. Journal of the Franklin Institute 356(18): 11364-11384. DOI: 10.1016/j.jfranklin.2019.01.056

Sun GH, Ma ZQ (2017) Practical tracking control of linear motor with adaptive fractional order terminal sliding mode control. IEEE/ASME Transactions on Mechatronics 22(6): 2643-2653. DOI:10.1109/TMECH.2017.2766279

Sun GH, Wu LG, Liu JX (2018) Practical tracking control of linear motor via fractional-order sliding mode. Automatica 94: 221-235. DOI:10.1016/j.automatica.2018.02.011

Tarbouriech S, Turner M (2009) Anti-windup design: an overview of some recent advances and open problems. IET Control Theory and Applications 3(1): 1-19. DOI:10.1049/iet-cta:20070435

Tran MD, Kang HJ (2016) Adaptive terminal sliding mode control of uncertain robotic manipulators based on local approximation of a dynamic system. Neurocomputing 228: 231-240. DOI:10.1016/j.neucom.2016.09.089

Tyan F, Bernstein DS (2010) Anti-windup compensator synthesis for systems with saturation actuators. International Journal of Robust & Nonlinear Control 5: 521-537

Wang N, Song JL, Dong Q (2024) Structural design of a wave-adaptive unmanned quadramaran with independent suspension. IEEE Transactions on Intelligent Transportation Systems 25(9): 12395-12406. DOI:10.1109/TITS.2024.3375278

Wang N, Zhang YH, Ahn CK, Xu QY (2022) Autonomous pilot of unmanned surface vehicles: bridging path planning and tracking. IEEE Transactions on Vehicular Technology 71(3): 2358-2374. DOI:10.1109/TVT.2021.3136670

Wang YJ, Zhao R, Zuo ZQ, Guan SY, Li HC (2021) Event-triggered dynamic anti-windup augmentation for saturated systems. International Journal of Systems Science 51(1): 196-216. DOI: 10.1080/00207721.2020.1823519

Wang YY, Luo GS, Gu LY, Li XD (2016) Fractional-order nonsingular terminal sliding mode control of hydraulic manipulators using time delay estimation. Journal of Vibration and Control 22(19): 3998-

4011. DOI:10.1177/1077546315569518

Wu GX, Ding Y, Tahsin T, Atilla I (2023) Adaptive neural network and extended state observer-based non-singular terminal sliding modetracking control for an underactuated USV with unknown uncertainties. Applied Ocean Research 135: 103560. DOI:10.1016/j.apor.2023.103560

Wu XR, Huang YY (2021) Adaptive fractional-order non-singular terminal sliding mode control based on fuzzy wavelet neural networks for omnidirectional mobile robot manipulator. ISA Transactions 121: 258-267. DOI:10.1016/j.isatra.2021.03.035

Yang YN, Yan Y (2016) Neural network approximation-based nonsingular terminal sliding mode control for trajectory tracking of robotic airships. Aerospace Science and Technology 54: 192-197. DOI:10.1016/j.ast.2016.04.021

Yin C, Chen YQ, Zhong SM (2014) Fractional-order sliding mode based extremum seeking control of a class of nonlinear systems. Automatica 50(12): 3173-3181. DOI: 10.1016/j.automatica.2014.10.027

Yu ZQ, Zhang YM, Jiang B, Fu J, Jin Y, Chai TY (2020) Composite adaptive disturbance observer-based decentralized fractional-order fault-tolerant control of networked UAVs. IEEE Transactions on Systems Man Cybernetics-Systems 52(2): 799-813. DOI: 10.1109/TSMC.2020.3010678

Zhang XK (2016) Robust control of longitudinal motion for hydrofoils based on nonlinear feedback. Navigation of China 39(1): 60-63, 73